SINGLE-MOLECULE STUDIES OF INTERMOLECULAR KINETICS USING NANO-ELECTRONICS CIRCUITS

A Dissertation
Submitted to the Graduate Faculty
of the
North Dakota State University
of Agriculture and Applied Science

By

James Steven Froberg

In Partial Fulfillment of the Requirements
for the Degree of
DOCTOR OF PHILOSOPHY

Major Department:
Physics

March 2020

Fargo, North Dakota

North Dakota State University
Graduate School

Title

SINGLE-MOLECULE STUDIES OF INTERMOLECULAR KINETICS USING NANO-ELECTRONICS CIRCUITS

By

James Steven Froberg

The Supervisory Committee certifies that this ***disquisition*** complies with North Dakota State University's regulations and meets the accepted standards for the degree of

DOCTOR OF PHILOSOPHY

SUPERVISORY COMMITTEE:

Yongki Choi
Chair

Erik Hobbie

Alan Denton

Sanku Mallik

Approved:

4/6/2020
Date

Sylvio May
Department Chair

ABSTRACT

As science and medicine advance, it becomes ever more important to be able to control and analyze smaller and smaller bioparticles all the way down to single molecules. In this dissertation several studies aimed at improving our ability to manipulate and monitor single biomolecules will be discussed.

First, we will discuss a study on developing a way to map dielectrophoresis with nanoscale resolution using a novel atomic force microscopy technique. Dielectrophoresis can be applied on nanoparticles through micron-scale electrodes to separate and control said particles. Therefore, this new method of mapping this force will greatly improve our ability to manipulate single biomolecules through dielectrophoresis.

The next two studies discussed will be aimed at using carbon nanotube nanocircuits to monitor single protein kinetics in real time. Drug development and delivery methods rely on the precise understanding of protein interactions, thus creating the need for information on single protein dynamics that our techniques provides. The proteins studied in these sections are MMP1 and HDAC8, both of which are known targets of anti-cancer drugs.

Finally, we developed a new strategy for diagnosing pancreatic cancer. Our strategy involves using graphene nanotransistors to detect exosomes released from the pancreatic tumor. The ability to reliably diagnose pancreatic cancer before it reaches metastasis would greatly improve the life expectancy of patients who develop this condition. We were able to test our technique on samples from a number of patients and were successfully able to distinguish patients with pancreatic cancer from noncancerous patients.

ACKNOWLEDGMENTS

I would like to acknowledge the many people who helped significantly with the completion of this dissertation. First off, I would like to thank Dr. Choi, who mentored me extensively throughout my time at NDSU, and without whom the research presented here would not have been possible. I would also like to thank all the other people in Dr. Choi's lab group who have helped me make it through grad school and assisted with my work. These people include Lina Alhalhooly, Myungkeun Oh, Woo-Sik Choi, and Dr. Woo.

Dr. Sanku Mallik has also contributed significantly to the completion of this work with his knowledge of pharmaceuticals and biology. Many students from Dr. Mallik's group also gave a lot of help by growing the exosomes, and other biomaterials used in this work. Fataneh Karandish especially did a lot of work in this area and was a key factor in getting first place in the 2017 NDSU Innovation Challenge. Other students who helped grow biomaterials for my work include Matthew Confeld, Jessica Pullan, and Tayebeh Anajafi. Additionally, I would like to thank Dr. D. K. Srivastava who provided us with proteins (MMPs and HDAC8), substrates and inhibitors used in this work.

I am also going to thank Prof. Philip Collins at UC Irvine for supplying SWNT-FET nano-devices, and our collaborator, Dr. Brett Goldsmith (Cardea Bio) for supplying graphene devices.

This research was supported financially by the NDSU startup, the NSF EPSCoR New Faculty grant, the ND NASA EPSCoR RID Awards, NDEPSCoR Doctoral Dissertation Award (DDA) and NIGMS NIH (R15GM122063 and P30GM103332).

Finally, I would like to thank the NDSU Physics Department including the professors, other students, Patty and Paul, for assisting me through grad school and making the time here enjoyable.

DEDICATION

This dissertation is dedicated to friends and family.

TABLE OF CONTENTS

LIST OF TABLES

LIST OF FIGURES

CHAPTER 1. INTRODUCTION AND BACKGROUND

1.1. Dissertation Introduction and Background

The ability to monitor and manipulate nanoscale biomaterials is essential for many areas of medicine including drug design (1,2), disease biomarker detection (3), and bioparticle separation (4-8). There is a wide variety of techniques available for this purpose including Förster resonance energy transfer (FRET) (9) and x-ray crystallography (10).

While all of these techniques can be used to acquire important information or control biological nano-particles, they all have some drawbacks. Specifically, optical and fluorescence methods are limited by population averaging and fluorophore bleaching effects that make distinguishing individual biomaterial kinetics impossible (11,12). Meanwhile, crystallography methods have limited ability to measure dynamics. To get around these issues an increasing amount of attention has been given to single-molecule nano-electronic methods (3,13). Specifically, in this thesis, the focus will be given to carbon material (graphene or carbon nanotube) based nanocircuits and their use in detecting and monitoring bioparticles. These devices allow for precise measurements of single-particle interactions at an extremely high bandwidth and for long time measurements (on the order of hours), while sidestepping the population averaging and bleaching effects discussed earlier.

Nano-electronic techniques basically involve applying bias through nanoscale materials and monitoring conductance through the materials. Thus, there is a force because of the applied bias (AC or DC). Depending on if the bioparticles are either metal or dielectric, force could be electrophoresis or dielectrophoresis. So, it is important to know how the field in the device influences the detection capability. Furthermore, nanoelectronics are also being investigated for their ability to sort bio-particles through dielectrophoresis. This method involves applying an AC

field to an array of micro to nano-scale electrodes to separate particles by a variety of parameters (4-8).

The focus of this thesis will be on nano-electronic circuits and their use in biological applications. The first chapter will focus on how the electric field applied by AC or DC bias to a nano-electronic device is distributed and influences the detection of single molecule interactions. Specifically, this chapter will focus on the distribution and effects of dielectrophoresis, starting by explaining the background theory and then discussing a novel method of measuring dielectrophoretic forces exerted on a particle by an electrode array using a new form of atomic force microscopy (AFM) (14,15) (AFM techniques are typically used for measuring surface characteristics and particle size, often used in fields such as drug delivery (16-20)), where the AFM tip is used to simulate a single bioparticle being acted on by dielectrophoresis. The second chapter focuses on the theory behind the electronic properties of transistors built using carbon nanotubes and graphene. This will be followed by two chapters discussing two different studies performed with carbon nanotube field effect transistors to monitor the single protein kinetics of MMP (chapter 3) (21) and HDAC8 (chapter 4) (22). Chapter 5 will then present research involving the detection of pancreatic cancer exosomes using graphene field-effect transistors (23). Finally, Chapter 6 will be the conclusion.

1.2. References

1. J. Banerjee, A. J. Hanson, B. Gadam, A. I. Elegbede, S. Tobwala, B. Ganguly, A. V. Wagh, W. W. Muhonen, B. Law, J. B. Shabb, D. K. Srivastava and S. Mallik, Bioconjugate Chemistry, 2009, 20, 1332-1339.

2. J. Banerjee, A. J. Hanson, E. K. Nyren-Erickson, B. Ganguli, A. Wagh, W. W. Muhonen, B. Law, J. B. Shabb, D. K. Srivastava and S. Mallik, Chemical Communications, 2010, 46, 3209-3211.

3. A. K. Manoharan, S. Chinnathambi, R. Jayavel, N. Hanagata, Science and Technology of Advanced Materials, 2016, 18, 43-50.

4. R. Pethig, Crit. Rev. Biotechnol, 1996, 16, 331–348.

5. H. Morgan, M. P. Hughes, and N. G. Green, Biophys. J, 1999, 77, 516–525.

6. H. Li and R. Bashir, Sens. Actuators B, 2002, 86, 215–221.

7. C.-F. Chou, J. O. Tegenfeldt, O. Bakajin, S. S. Chan, E. C. Cox, N. Darnton, T. Duke, and R. H. Austin, Biophys. J, 2002, 83, 2170–2179.

8. M. Washizu and O. Kurosawa, IEEE Trans. Ind. Appl, 1990, 26, 1165–1172.

9. S. Matsumoto, G. G, Hammes, Biochemistry, 1975, 14, 2, 214-224.

10. J.-P. Xiong, T. Stehle, R. Zhang, A. Joachimiak, M. Frech, S. L. Goodman, M. A. Arnaout, Science, 2002, 296, 5565, 151-155.

11. Y. Choi, I. S. Moody, P. C. Sims, S. R. Hunt, B. L. Corso, D. E. Seitz, L. C. Blaszcazk, P. G. Collins and G. A. Weiss, J. Am. Chem. Soc., 2012, 134, 2032.

12. M. V. Akherov, Y. Choi, T. J. Olsen, P. C. Sims, M. Iftikhar, O. T. Gul, B. L. Corso, G. A. Weiss, P. G. Collins, ACS Chem. Biol., 2015, 10, 1495-1501.

13. A. V. Vlassoz, S. Magdaleno, R. Setterquist, R. Conrad, Biochimica et Biophysica Acta (BBA)-General Subjects, 2012, 1820, 940-948.

14. J. Froberg, V. Jayasooriya, S. You, D. Nawarathna, Y. Choi, Applied Physics Letters, 2017, 110, 203701.

15. J. Froberg, M. Oh, V. Jayasooriya, D. Nawarathna, Y. Choi, "*Atomic Force Microscopy in Dielectrophoresis Applications"* in Atomic Force Microscopy: Principles, Developments and Applications, Nova Publishers, 21-46, 2018

16. T. Anajafi, J. Yu, A. Sedigh, M. Haldar, W. Muhonen, S. Oberlander, H. Wasness, J. Froberg, S. Molla, K. Katti, Y. Choi, J. Shabb, D. Srivastava, S. Mallik, Molecular Pharmaceutics, 2017.

17. Y. Pan, S. Neupane, J. Farmakes, M. Bridges, J. Froberg, J. Rao, S. Qian, G. Liu, Y. Choi, Z. Yang, Nanoscale, 2017, 9, 3512-3523.

18. L. Xia, K. Kumar, J. Froberg, P. Kulkarni, K. Gange, Y. Choi, S. Mallik, K. Sarkar, Ultrasound in Medicine and Biology, 2017, 44, 447-457.

19. J. Osborn, J. Pullan, J. Froberg, Y. Choi, S. Mallik, The Journal of the Acoustical Society of America, 2019.

20. F. Karandish, J. Froberg, P. Borowics, J. Wilkinson, Y. Choi, S. Mallik, Colloids and Surfaces B: Biointerface, 2017.

21. J. Froberg, W. Choi, A. Seddigh, T. Anajafi, J. Farmakes, Z. Yang, S. Mallik, D. Srivastava, Y. Choi, Chemical Communications, 2018.

22. S. You, J. Froberg, J. Yu, M. Haldar, A. Sedigh, S. Mallik, Y. Choi, Chemical Communications, 2017, 53, 3307-3310. https://pubs.rsc.org/en/content/articlelanding/2018/cc/c8cc04601h

23. S. Woo, J. Froberg, Y. Pan, S. Tani, B. R. Goldsmith, Z. Yang, Y. Choi, Applied Electronic Materials, 2020. https://pubs.rsc.org/en/content/articlelanding/2017/cc/c6cc09949a#!divAbstract

CHAPTER 2. QUANTITATIVE MEASUREMENTS OF DIELECTROPHORESIS IN A NANOSCALE ELECTRODE ARRAY WITH AN ATOMIC FORCE MICROSCOPY[1]

2.1. Dielectrophoresis Introduction

Dielectrophoresis (DEP) describes a force experienced by a suspended polarizable particle in a non-homogeneous electric field toward the direction of the field gradient (1-6). This phenomenon arises from basic electrostatics (5,7); if a polarizable particle is placed in an electric field it will become electrically polarized along the direction of the electric field. If this occurs in a uniform electric field, both poles of the particles will experience equal but opposite forces so that the particle remains in its current state (7). However, if the electric field is non-uniform, a greater force will be applied to the pole towards the stronger electric field, and the particle will move in the direction of the field gradient (Fig. 2.1).

The force experienced by this particle depends strongly on the polarizability of both the particle itself and the medium it is suspended in, as well as the magnitude and direction of the electric field. Additionally, DEP can occur in AC electric fields wherein the direction of the force depends on the frequency of the electric field and the polarizability of the suspended particle compared to that of the medium (1,8,9). Due to the strong dependence of DEP on the material properties of the particle, DEP has gained much attention in its ability to selectively manipulate biological-particles such as cells proteins, cells, RNA and DNA (10-22).

[1] The material in this chapter was co-authored by James Froberg, V. Jayasooriya, S. You, D. Nawarathna, M. Oh, and Yongki Choi. James Froberg was primarily responsible for experimental design, collecting data, analyzing data and drawing conclusions from the results.

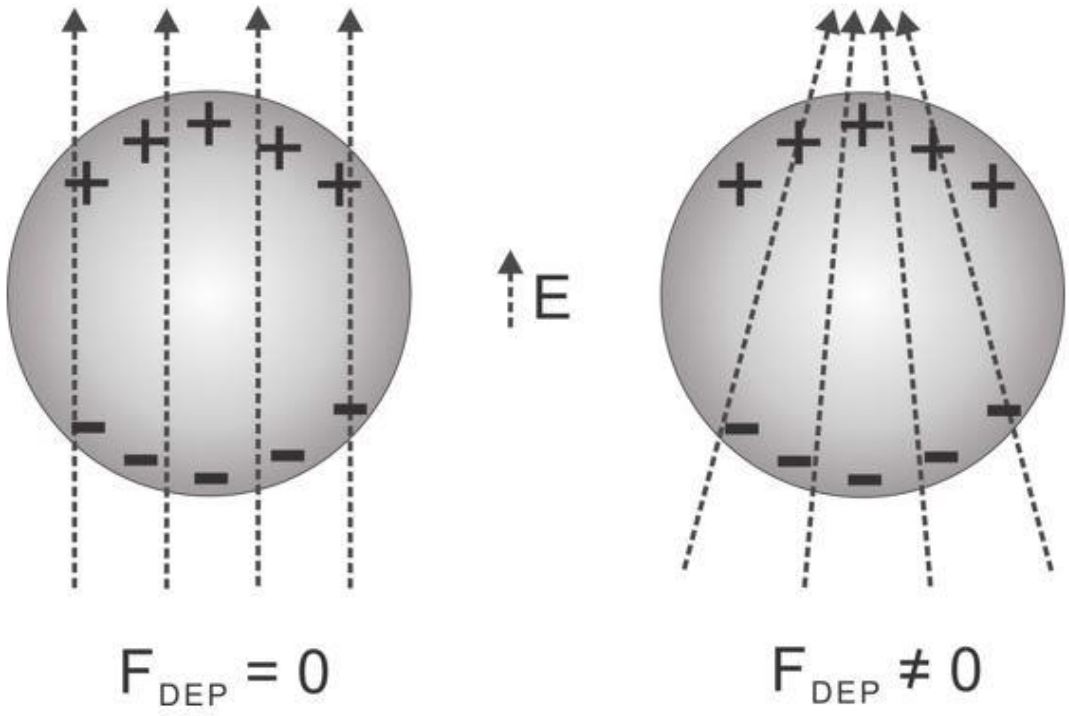

Fig. 2.1: A dielectric particle becomes polarized in an electric field in the direction of the field. If the field is uniform, the positive and negative poles of the particle experience equal and opposite forces so that no net force is experienced by the particle. On the other hand, if the field is non-uniform, the particle experiences a net force in the direction that the field is stronger.

2.2. Dielectric Sphere

In order to gain a better sense of how DEP works, we will now go through an example with a dielectric sphere suspended in a medium permeated by an electric field, as can be seen in Figure 2.1. First, we will analyze the case of the sphere on the left, in the uniform electric field. In this case, the electric field polarizes the sphere into a dipole, and thus, it experiences a dipole force that can be expressed as:

$$\bar{F}_{Dipole}(t) = \bar{P}_{eff} \cdot \nabla \bar{E} \tag{2.1}$$

Where $\bar{F}_{Dipole}(t)$ is the dipole force, $\bar{P}_{eff}$ is the effective dipole moment, and $\bar{E}$ is the electric field (1,7). The effective dipole moment of a dielectric sphere in a dielectric medium, can be expressed as:

$$\bar{P}_{eff} = 4\pi\varepsilon_1 K R^3 E \tag{2.2}$$

Where ε_1 is the permittivity of the medium, R is the radius of the sphere, E is the magnitude of the electric field, and K is the Clausius-Mossotti function (1,4) that can be written in terms of the permittivity of the medium, and the permittivity of the sphere, ε_2.

$$K = \frac{\varepsilon_2 - \varepsilon_1}{2\varepsilon_1 + \varepsilon_2} \tag{2.3}$$

Equations 2.1-2.3 can then be combined to obtain the force being applied to the particle by dielectrophoresis:

$$\bar{F}_{DEP} = 2\pi\varepsilon_1 R^3 \left(\frac{\varepsilon_2 - \varepsilon_1}{2\varepsilon_1 + \varepsilon_2}\right) \nabla E^2 \tag{2.4}$$

This expression depends on the electric field gradient, not the actual magnitude of the field. Thus, a sphere in a uniform electric field does not experience a force from DEP. Additionally, the DEP force depends on the permittivity of both the sphere and the medium. Positive dielectrophoresis occurs if the sphere's permittivity is greater than the medium's. In these conditions, the particle will be attracted to maxima of the electric field. If the opposite is true, and the medium has a greater permittivity than the particle, the particle will be attracted towards minima in the electric field. This is known as negative dielectrophoresis. In the case that both the sphere and the medium are conductive, the permittivities, ε_1 and ε_2, can simply be replaced with the conductivities, σ_1 and σ_2. However, if both the sphere and the medium are dielectric, and an AC electric field is being applied, complex higher order terms must be used for the permittivities (1,4).

$$\varepsilon \to \varepsilon' - j\varepsilon'' + \frac{\sigma}{jw} \tag{2.5}$$

Which leads to a new expression for K(w) (4), ignoring dielectric loss (or, $\varepsilon' = 0$).

$$K = \frac{\varepsilon_2 - \varepsilon_1 - j(\sigma_2 - \sigma_1)/w}{\varepsilon_2 + 2\varepsilon_1 - j(\sigma_2 + 2\sigma_1)/w} \tag{2.6}$$

This means that DEP force depends on the frequency of the applied electric field. In addition, the fluid that the sphere is suspended in usually has a high enough viscosity to dampen all motion except that due to the time-averaged force. The time-averaged DEP force can be expressed as:

$$\langle \bar{F}_{DEP} \rangle = 2\pi\varepsilon_1 R^3 \mathrm{Re[K(w)]} \nabla E_{rms}^2 \tag{2.7}$$

Where E_{rms} is the root mean square of the electric field and the time-averaged force only depends on the real part of K. After much simplifying, the real part of K reduces to:

$$Re[K] = \frac{\varepsilon_2 - \varepsilon_1}{\varepsilon_2 + 2\varepsilon_1} + \frac{3(\varepsilon_1\sigma_2 - \varepsilon_2\sigma_1)}{\tau_{MW}(\sigma_2 + 2\sigma_1)^2(1 + w^2\tau_{MW}^2)} \tag{2.8}$$

$$\tau_{MW} = \frac{\varepsilon_2 + \varepsilon_1}{\sigma_2 + 2\sigma_1} \tag{2.9}$$

τ_{MW} is the Maxwell-Wagner charge relaxation time, and represents the rate at which charges redistribute from a dipole on the particle's surface (4). From equation 2.8, two cases can be considered. In the first case, where $\sigma_2 < \sigma_1$ and $\varepsilon_2 > \varepsilon_1$, if the frequency is high, the term on the right side goes to zero and the term on the left is positive so that $Re[K]$ is positive which leads to the time-averaged DEP force being positive. When the frequency is low, the term on the right dominates, and some simplification leads to $Re[K]$ becoming:

$$Re[K] = \frac{\sigma_2 - \sigma_1}{\sigma_2 + 2\sigma_1} \tag{2.10}$$

Since $\sigma_2 < \sigma_1$, this term is negative and the time-averaged DEP force becomes negative. Inversely, if $\sigma_2 > \sigma_1$ and $\varepsilon_2 < \varepsilon_1$, the same terms dominate for high and low frequencies, but their signs are switched so that the time-averaged DEP force is negative for high frequencies and positive for low frequencies. Figure 2.2 shows how $Re[K]$ depends on the frequency of the electric field for both of these cases.

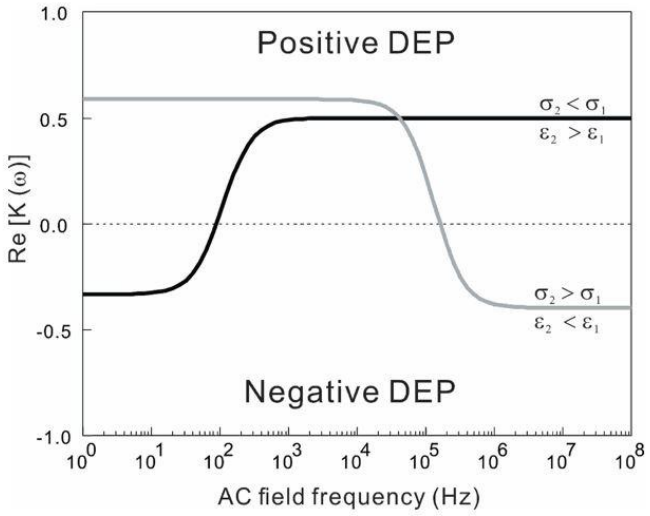

Fig. 2.2: Real part of the Clausius-Mossotti function and polarity of DEP as function of AC field frequency. In calculating this plot, the following parameters were used: $\varepsilon_p = 11.68\varepsilon_o$, $\varepsilon_m = 79\varepsilon_o$, $\sigma_p = 9\times10^{-4}$ S/m, $\sigma_m = 2\times10^{-4}$ S/m for the gray curve, and $\varepsilon_p = 10\varepsilon_o$, $\varepsilon_m = 2.5\varepsilon_o$, $\sigma_p = 10^{-8}$ S/m, $\sigma_m = 4\times10^{-8}$ S/m for the black curve.

2.3. Non-Spherical Particles

Although many DEP applications involve the manipulation of spherical particles such as cancer cells and exosomes, it is also widely used for manipulating particles that are elliptical (10,11,13,19,23-25). Later in this chapter we will be discussing how an AFM tip can be used to measure DEP forces. In this case, the AFM tip is more accurately represented as a prolate spheroid. In this section, we will be analyzing the DEP force felt by two extreme elliptical cases, the prolate spheroid (needle-shaped) and the oblate spheroid (disc shape).

In order to calculate the DEP force in both of these cases, we will start with the general equation for DEP force applied to an ellipse. This equation can be calculated by finding the effective dipole moment and applying it to equation 2.2,

$$\bar{F}_{DEP} = \frac{4\pi abc(\varepsilon_2-\varepsilon_1)}{3}\left[\frac{E_{0,x}}{1+\left(\frac{\varepsilon_2-\varepsilon_1}{\varepsilon_1}\right)L_x}\frac{d}{dx}+\cdots\right]\bar{E} \tag{2.11}$$

where $L_{x,y,z}$ are the polarization factors along each axis (25). In the case of the prolate spheroid, this becomes much simpler if the long axis of the spheroid is aligned parallel with axial

symmetry to the electric field, eliminating each term except that which contains the gradient in the direction of the long axis, or the z-axis. In addition, since b=c, the above equation simplifies quite a bit. Using $L_{\|}$ as the depolarization factor in the direction parallel with the electric field (4,25).

$$\bar{F}_{DEP} = \frac{4\pi ab^2}{3}\left[\frac{\varepsilon_2-\varepsilon_1}{1+\left(\frac{\varepsilon_2-\varepsilon_1}{\varepsilon_1}\right)L_{\|}}\right]\frac{dE_{0,z}^2}{dz}\hat{z} \tag{2.12}$$

This equation is similar to that of the spherical particle. The DEP force is still strongly dependent on the volume of the spheroid, and the difference between the particle and medium's permittivities. The same expression is true for the oblate spheroid, if it is aligned symmetrically with the electric field. If the spheroids are not aligned symmetrically with the electric field, this expression becomes much more complicated, however, the DEP force is still directly dependent on the volume and permittivities and can still be positive or negative depending on the frequency of the electric field.

2.4. Mapping Dielectrophoresis with Atomic Force Microscopy

2.4.1. Dielectrophoresis Introduction

Recent advances in biotechnology have allowed capturing individual biomolecules including disease-markers and cancer cells and monitoring their biological activities. (26–29) The ultimate goal of this field would be to completely control and manipulate the biomolecules for practical diagnostic applications. Among a number of techniques developed for the detection and manipulation of biomolecules, dielectrophoresis (DEP)-based methods have demonstrated the feasibility of a remote control of target molecules to trap and dissect for highly sensitive screening. For example, DEP has been used for the separation of yeast cells (14), viruses (15), and cancer cells (26,10), as well as to trap particular DNA molecules (1,4), providing tremendous potential in biomedical applications.

In principle, DEP is a force exerted on polarizable particles such as biomolecules and cells in the presence of non-uniform AC electric fields in a liquid medium (30). Depending on the dielectric responses of the particle and the surrounding medium, the external fields induce an effective dipole moment p on the particle and an instantaneous force $\bar{F}_{DEP} = \bar{P} \cdot \nabla \bar{E}$, acting on the dipole (31,32). For the particle suspended in the non-uniform fields, the net force does not vanish. Thus, spatially asymmetric force due to the inhomogeneous field gradient in the medium drives the movement of the particle. In general, the force can be used to selectively attract (attractive $\bar{F}_{DEP}$) or repel (repulsive $\bar{F}_{DEP}$) biomolecules of interest from a complex medium to regions of strong electric fields. For example, cancer cells (32), cellular components (26), and biomarkers (7,33) can be collected, separated, concentrated, and transported using DEP-based micro-fluidic devices.

2.4.2. Importance of Mapping Dielectrophoresis

Although such non-invasive, non-contact DEP manipulation is a promising platform for biomedical applications, measuring and determining the strength of $\bar{F}_{DEP}$ on biomolecules in nanoelectronic devices are challenging problems. In addition, several issues associated with DEP limit its applicability in practice. First, the external AC field intensity and its frequency to generate bipolar DEP can cause unwanted electrochemical reactions such as water electrolysis at metal electrodes (15), destroying both the biological sample and the nanoelectronic devices. Second, $\bar{F}_{DEP}$ may not be uniformly distributed in the electrodes patterned on the devices due to the high sensitivity of the field variations near the sharp corners or edges of the electrodes at the nanoscale (34). Effective solutions to the problems, on the other hand, would help to design the nanoelectronic device and tune the operating parameters to achieve strong $\bar{F}_{DEP}$ to effectively manipulate target biomolecules in a desired manner under physiological conditions.

2.4.3. Using an AFM to Measure Dielectrophoresis

Here, we show that $\bar{F}_{DEP}$ in the nanoelectronic devices can be experimentally measured and quantitatively evaluated by atomic force microscopy (AFM). A non-contact, dynamic AC lift-mode AFM method similar to the typical electric or magnetic force measurement methods (5,35) was used to investigate the force between an AFM probe tip and the nanoelectronic devices including both the smooth surface and the sharp edges of electrodes. The measurements allowed mapping out the force variation along the direction (z) normal to the electrode surface in the device. In this work, the conventional interdigitated electrode array that has proven to be quite useful for dielectrophoretic separation and travelling wave dielectrophoresis in previous research studies (36,37) was examined as shown in Fig. 2.3.

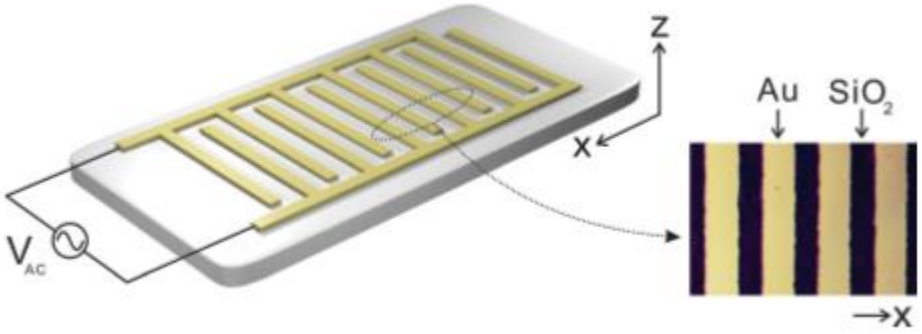

Fig. 2.3: Schematic of an interdigitated metal (Au) electrode array connected to the AC voltage source.

The device consists of planar metallic electrode arrays on a SiO_2 substrate. With a pre-patterned mylar mask, gold electrodes were defined by the standard optical lithography, similar to the previous study (38). The width of electrodes, gaps between the electrodes, and the height of the electrodes were 16µm, 10µm, and 140nm, respectively.

Devices were mounted in a liquid-compatible commercial AFM (NT-MDT NTEGRA AFM), and the AFM imaging was performed in an ionic buffer solution without evaporation

while measuring. Conventional silicon AFM probe tips without a coating (force constant = 2.7N/m, Budget sensors) were used for the imaging. The external AC voltage between the two metal electrodes was applied by a commercial function/arbitrary waveform generator (Agilent 33220A), which was filtered and synchronized with the AFM scanning. A multi-pass scanning technique was employed for the precise measurements of both surface topography and the force gradient. The first-pass scanning was performed in the typical semi-contact mode to obtain the surface topography characteristics. During the second-pass measuring the force gradient, the probe was raised above the surface at a distance z followed by the surface topography contour. Such lift-mode scanning in the second-pass prevents any influence of surface features on the measurement.

The second-pass measurement depends solely on the force gradient along the z direction based on the point probe approximation assuming that the probe tip has a dipole moment located in the center of the tip end. The AC lift-mode operates with a lock-in feedback loop to keep driving the probe oscillation at nearly the resonance frequency (5,39). When a force acts on the probe tip, it causes the resonance frequency of the tip to shift, depending on the force gradient and the direction. Additionally, such changes in resonance frequency result in an amplitude and phase shift. Thus, although the three parameters serve as an indicator of the force measurement, the force gradient is mainly detected by measuring the probe tip's phase vibration in the amplitude modulation mode using a simple lock-in amplifier. A mathematical relationship between the phase shift and the force gradient when $\frac{\partial F}{\partial z}$ is very small in magnitude compared to k is given by

$$\Delta\emptyset = \frac{Q}{k}\frac{\partial F}{\partial z} \tag{2.13}$$

where Q is the Q-factor of the resonance peak, k is the force constant of the probe tip, and $\frac{\partial F}{\partial z}$ is the force gradient in the direction normal to the surface (40,8). When $\frac{\partial F}{\partial z}$ is measured according to z, F can be obtained by integrating $\frac{\partial F}{\partial z}$. For example, the negative shift of the measured phase corresponds to the attractive F and negative $\frac{\partial F}{\partial z}$ along the z direction. The AFM measurements were carried out in a phosphate buffer (1–10μM KH_2PO_4, pH 7) at room temperature. The ionic strength of the buffer and the amplitude and frequency of the applied AC voltage were determined by the classical Maxwell-Wagner (MW) theory (30,31). Specifically, the complex Clausius-Mossotti (CM) factor depending on the complex permittivities of the particle and suspending medium and a depolarizing factor of the particle allow estimating the frequency dependent effective dipole moments of the particles as well as the magnitude and polarity of $\bar{F}_{DEP}$ (see Figs. 2.4 and 2.5).

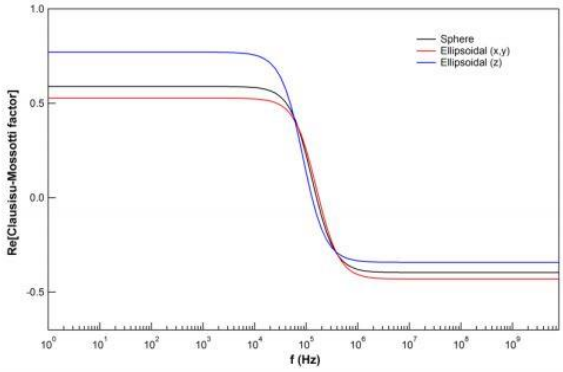

Fig. 2.4: Real part of the CM factor. In calculating this plot, the following parameters were used: a = b = c = 20 nm and Lx = Ly = Lz = 1/3 for the sphere case, a = b = 65 nm, c = 140 nm, Lx = 0.41, Ly = 0.41, Lz = 018 for the ellipsoidal case, εp = 11.68εo, εm = 79εo, σp= 9×10-4 S/m, σm= 2×10-4 S/m for both cases.

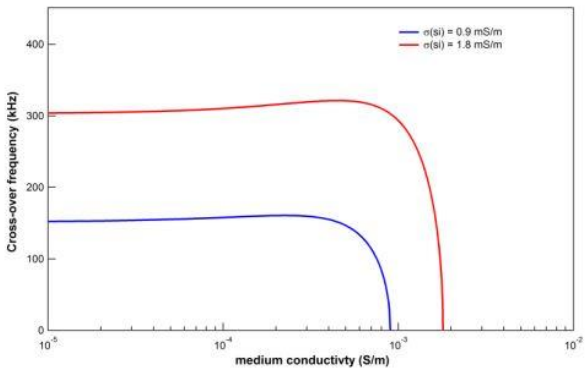

Fig. 2.5: Cross-over frequency dependence to the medium conductivity of buffer at two different conductivities of the particle. The values of 9×10-4 S/m and 18×10-4 S/m are the internal conductivity of Si and the internal conductivity with surface conductivity, respectively.

2.4.4. Mapping Dielectrophoresis Using an AFM

Figure 2.6 depicts typical multi-pass AFM images of the device in the absence and in the presence of the external AC fields (V_{ac}). Figure 2.6(a) presents a topography image and the corresponding height profile of the device acquired during the first-pass scanning, while the Vac was in the off-mode.

The metal electrodes and SiO_2 substrates were relatively flat and smooth compared to the sharp edge of the electrodes in the image. The edge line of the electrode is highly disordered at the nanoscale, producing additional non-uniform electric field distributions due to the lighting rod effects (34). During the second-pass, lift-mode scanning at a particular z, a sinusoidal wave form of V_{ac} with a peak to peak potential of 5V is applied through the two electrodes (Fig. 2.3) to examine the AC field effects. Figure 2.6(b) shows the phase images of the same electrode (Fig. 2.6(a)) under three different conditions: V_{ac} (5 V_{pp}, 10kHz); V_{ac} (0V, GND); and V_{ac} (5 V_{pp}, 5MHz) at z = 20nm.

In the control measurements performed without the external AC field (V_{ac} = 0 V), the phase shift was observed along the electrode edge direction. Such a phase shift is attributed to a geometry effect at the sharp step edge. When the AFM scans over the step edge, the distance z

between the tip and the sample instantly decreases and brings the tip into a more negative force gradient until the feedback loop restores the initial distance z (39). Therefore, the negative force gradient due to the attractive force variations is shown in the dark color phase image only at the edge.

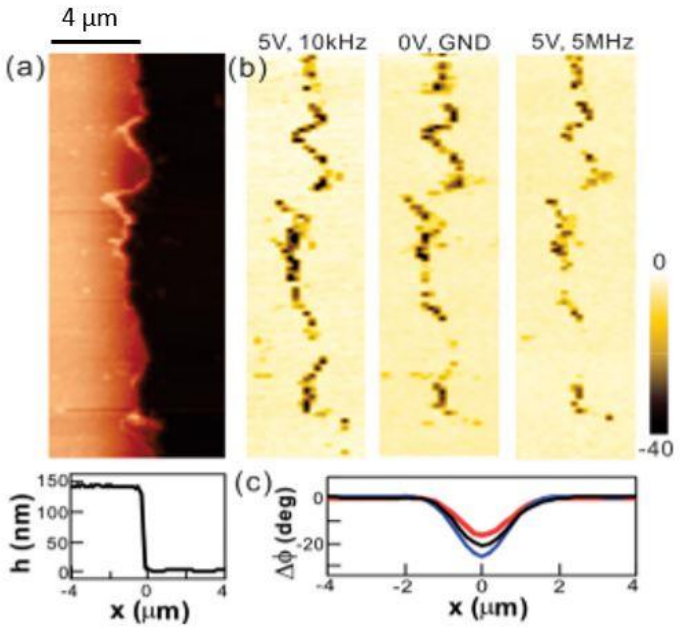

Fig. 2.6: Multi-pass AFM measurements. (a) A topography image of the metal electrode (red color) and the SiO2 (black color) substrate and a height profile of line-cuts of the cross-section. (b) Phase images of (a) at three Vac fields. (c) The averaged phase shifts along the electrode step edge. Blue, black, and red curves correspond to 10 kHz, GND, and 5MHz fields, respectively.

When the AC electric fields were applied with different frequencies, further phase shifts were observed as depicted in Fig. 2.6(b). In the presence of V_{ac} (10 kHz), the features along the edge line in the phase image were unchanged, but their color was revealed to be darker, reflecting additional attractive forces acting on the AFM tip. Thus, the low frequency AC fields generated the attractive $\bar{F}_{DEP}$ and negative $\partial\bar{F}_{DEP}/\partial z$. In contrast, repulsive $\bar{F}_{DEP}$ generated by the high frequency (5MHz) fields reduced the net force, resulting in the brighter edge line in Fig. 2.6(b). Figure 2.6(c) compares the mean phase shift along the edge direction for each

measurement. Taken together, the frequency dependent, binary $\bar{F}_{DEP}$ effects were able to be measured by our multi-pass AFM experiments.

2.4.5. Dielectrophoresis Spacing Distribution

To examine the spatial distribution of $\bar{F}_{DEP}$ and $\partial\bar{F}_{DEP}/\partial$z along the x and z directions, the AFM measurements were carried out by varying z across the electrodes with two fixed frequencies of 10kHz (attractive $\bar{F}_{DEP}$) and 5MHz (repulsive $\bar{F}_{DEP}$). Figure 2.7(a) displays pure $\partial\bar{F}_{DEP}/\partial$z components and their z dependence, where the background component without the AC fields was removed at each z. Both positive and negative $\partial\bar{F}_{DEP}/\partial$z peaked at the edge of the electrode (x = 0) for all z. The magnitude of $\partial\bar{F}_{DEP}/\partial$z fell off along the x axis regardless of the sign of $\partial\bar{F}_{DEP}/\partial$z and z, suggesting the reduction in the field strength variations along the x axis.

Finally, the magnitude of $\partial\bar{F}_{DEP}/\partial$z approached minimum values when the tip was away from the edge ($|x|$>0), indicating minimum points in the field strength at the top of the electrode and a point equidistant between two electrodes. Such observations are in excellent agreement with the strong dependence of $\bar{F}_{DEP}$ on the strength of field gradients

$$(\bar{F}_{DEP} \propto \nabla E^2) \tag{2.14}$$

Figure 2.7(b) displays the peak values of $\partial\bar{F}_{DEP}/\partial$z and $\bar{F}_{DEP}$ calculated from the measured $\partial\bar{F}_{DEP}/\partial$z as a function of z (5). The values were nonlinearly decreased upon increasing the separation distance z between the tip and the electrode edge. The shape of these curves suggests the nonlinear changes in the intensity of the field gradient at the edge. Furthermore, the magnitude of $\bar{F}_{DEP}$ and $\partial\bar{F}_{DEP}/\partial$z was almost identical for two different frequencies at the same z. The results indicate that the CM factors for the low (10 kHz) and high (5 MHz) frequencies are nearly identical, which is further supported by our CM calculation (Fig. 2.4). When the tip was

further away from the edge (>80nm), $\bar{F}_{DEP}$ approached nearly zero, providing an upper limit for the working distance of the short-range $\bar{F}_{DEP}$.

2.4.6. COMSOL Modeling of Dielectrophoresis

Commercial finite element software, COMSOL Multiphysics (COMSOL, Inc.), was used to generate plots of the electrical field distribution in the electrodes and details of the software have been published elsewhere (13). To set-up COMSOL simulations, briefly, Interdigitated Electrodes (IDEs) were drawn to a scale using AutoCAD (Autodesk) software and imported into COMSOL software. We then used the AC/DC electric current (EC) module and frequency domain studies to calculate electric fields and the electric field gradients. Furthermore, we assumed that a buffer solution (σm= 2×10-4 S/m and εm = 79εo at 0 Hz) was filled over the IDEs (As used in the experiments) and also assumed that IDEs were connected to the external function generator with output of sinusoidal potential (5 V peak to peak and 10 kHz). Finally, the IDEs were meshed using free triangular extremely fine mesh with maximum element size of 0.64 μm and minimum element size of 1.28 nm. Using this information, we calculated the magnitude of the electric field (E) and electric field gradient (∇E 2) across the electrodes as shown in the Fig. 2.8. The large variations in the fields appeared at the sharp edge, which was in strong agreement with our experimental observations. An asymmetric shape of the gradient of the field is due to the non-uniform charge distribution near the electrode edge. Furthermore, the magnitude of field gradients decreases as z increases, confirming the separation distance-dependent, short-range DEP that is observed experimentally.

Previous studies performed with both micro-scale particles and electrodes have revealed that $\bar{F}_{DEP}$ was sufficient to drive motions of the particles (41). When the particle size decreases to the nanoscale, however, $\bar{F}_{DEP}$ substantially decreases due to the particle volume dependence of

$\bar{F}_{DEP}$ ($\bar{F}_{DEP} \propto R^3$). Thus, although $\bar{F}_{DEP}$ can be either repulsive or attractive by the driving frequency of the fields, our results proved that the strength and the apparent working distance of $\bar{F}_{DEP}$ were strongly dependent on both particles' dimension and electrodes' fine structure.

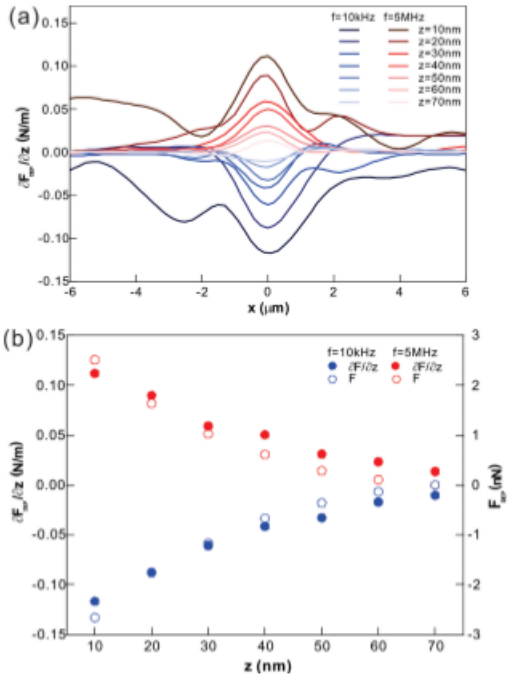

Fig. 2.7: The spatial distribution of $\partial\bar{F}_{DEP}/\partial$z. (a) The average $\partial\bar{F}_{DEP}/\partial$z versus two driving (10kHz and 5MHz) frequencies, demonstrating attractive $\bar{F}_{DEP}$ with 10kHz and repulsive $\bar{F}_{DEP}$ with 5MHz. (b) The average $\partial\bar{F}_{DEP}/\partial$z and $\bar{F}_{DEP}$ versus the separation distance z. $\bar{F}_{DEP}$ was obtained by integrating $\partial\bar{F}_{DEP}/\partial$z.

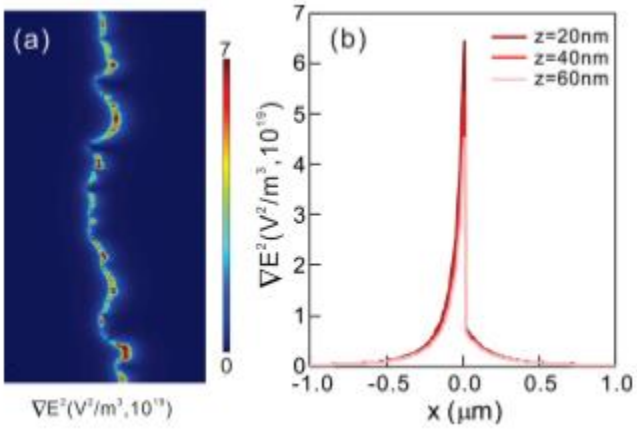

Fig. 2.8: Simulation images generated by COMSOL Multiphysics. (a) A plot of the gradient field strength in two dimensions. (b) The profile of (a) at different z values along the x direction.

2.5. Summary of Mapping Dielectrophoresis

In conclusion, we achieved quantitative measurements of $\bar{F}_{DEP}$ and $\partial\bar{F}_{DEP}/\partial$z in conventional, nanoscale, electronic devices using the multi-pass AFM methods. The results provided the spatial distribution of DEP and its strong dependence on the nanoscale structure of the electrode and the nanoscale separation distance from the electrode edge. On this scale, precise measurements of DEP are more important for quantitative comparisons among the competing forces such as viscous drag, Brownian, and hydrodynamic forces to determine the dominant forces governing the movements of biomolecules. Thus, the present study could benefit further development of DEP-based sensors and detectors for nanoscale proteins and biomarkers. For example, DEP could be integrated with conventional field effect transistor-based biosensors to lower the detection limit of target molecules on a rapid timescale. Alternatively, DEP could be used to prescreen and filter the target/non-target molecules in microfluidic devices to maximize detection sensitivity or minimize interference from the non-target molecules in the blood sample. The development of such techniques demands precise knowledge of DEP to design nanoelectronic devices and tune the operating parameters associated with other interfering forces for the effective manipulation of the target molecules.

2.6. References

1. H. A. Pohl, *Dielectrophoresis: The Behavior of Neutral Matter in Nonuniform Electric Fields* (Cambridge University Press, Cambridge, 1978).
2. J. Voldman, Annu. Rev. Biomed. Eng, 2006, 8, 425–454.
3. T. B. Jones, IEEE Eng. Med. Biol, 2003, 22, 33–42.
4. 1T. B. Jones, *Electromechanics of Particles* (Cambridge University Press, Cambridge, 1995).

5. A. Ramos, H. Morgan, N. G. Green, and A. Castellanos, J. Phys. D: Appl. Phys, 1998, 31, 2338.

6. Y. Kang, D. Li, S. A. Kalams, J. E. Eid, Biomedical Microdevices, 2008, 10, 243-249.

7. J. Jackson, *Classical Electrodynamics*, 3rd ed. (Wiley, 1998). R. Pethig, Critical Reviews in Biotechnology, 1996, 16, 331-348.

8. M.-T. Wei, J. Junio, and H. D. Ou-Yang, Biomicrofluidics, 2009, 3, 012003.

9. A. Kuzyk, B. Yurke, J. J. Toppari, V. Linko, P. Torma, Small, 2008, 4, 447-450.

10. M. Washizu and O. Kurosawa, IEEE Trans. Ind. Appl, 1990, 26, 1165–1172.

11. M. James, M. M. Alkaisi, J. J. Evans, J. Nagase, Japanese Journal of Applied Physics, 2005, 44, 5717.

12. D. V. Korneev, A. V. Popova, V. M. Generalov, B. N. Zaitsev, Biophysics, 2016, 61, 413-419.

13. L. Velmanickam, D. Laudenbach, and D. Nawarathna, Phys. Rev. E, 2016, 94, 042408.

14. H. Li and R. Bashir, Sens. Actuators, B, 2002, 86, 215–221.

15. C.-F. Chou, J. O. Tegenfeldt, O. Bakajin, S. S. Chan, E. C. Cox, N. Darnton, T. Duke, and R. H. Austin, Biophys. J, 2002, 83, 2170–2179.

16. B. P. Lynch, A. M. Hilton G. J. Simpson, Biophysical Journal, 2006, 91, 2678-2686.

17. K. Khoshmanesh, S. Baratchi, F. J. Tovar-Lopez, S. Nahavandi, D. Wlodkowic, A. Mitchell, K. Kalantar-zadeh, Microfluidics and Nanofluidics, 2012, 12, 597-606.

18. D. Nawathna, T. Turan, H. K. Wickramasinghe, Applied Physics Letters, 2009, 95, 083117.

19. F. F. Becker, X. B. Wang, Y. Huang, R. Pethig, J. Vykoukal, P. R. Gascoyne, Proceedings of the National Academy of Sciences, 1995, 92, 860-864.

20. J. An, J. Lee, S. H. Lee, J. Park, B. Kim, Analytical and Bioanalytical Chemistry, 2009, 394, 801-809.

21. W. H. Yeo, J. H. Chung, Y. Liu, K. H. Lee, The Journal of Physical Chemistry B, 2009, 113, 10849-10858.

22. G. G. Nicolas, B. J. Thomas, Journal of Physics D: Applied Physics, 2007, 40, 78.

23. H. N. Nili, G, Green, Physical Review E, 2014, 89, 063302.

24. A. Moroz, Journal of the Optical Society of America B, 2009, 26,517-527.

25. G. Zheng, F. Patolsky, Y. Cui, W. U. Wang, and C. M. Lieber, Nat. Biotechnol, 2005, 23, 1294–1301.

26. C. Joo, H. Balci, Y. Ishitsuka, C. Buranachai, and T. Ha, Annu. Rev. Biochem, 2008, 77, 51–76.

27. E. Stern, A. Vacic, N. K. Rajan, J. M. Criscione, J. Park, B. R. Ilic, D. J. Mooney, M. A. Reed, and T. M. Fahmy, Nat. Nanotechnol, 2010, 5, 138–142.

28. R. Pethig, Crit. Rev. Biotechnol, 1996, 16, 331–348.

29. H. Morgan, M. P. Hughes, and N. G. Green, Biophys. J, 1999, 77, 516–525.

30. P. R. C. Gascoyne and J. Vykoukal, Electrophoresis, 2002, 23, 1973–1983.

31. F. F. Becker, X. B. Wang, Y. Huang, R. Pethig, J. Vykoukal, and P. R. Gascoyne, Proc. Natl. Acad. Sci. U.S.A, 1995, 92, 860–864.

32. J.-R. Gong, Small, 2010, 6, 967–973.

33. Y. Martin and H. K. Wickramasinghe, Appl. Phys. Lett, 1987, 50, 1455–1457.

34. M. Nonnenmacher, M. P. O'Boyle, and H. K. Wickramasinghe, Appl. Phys. Lett, 1991, 58, 2921–2923.

35. M. Hywel, I. Alberto Garcia, B. David, G. G. Nicolas, and R. Antonio, J. Phys. D: Appl, 2001, Phys. 34, 1553.

36. L. Velmanickam, D. Laudenbach, and D. Nawarathna, Phys. Rev. E, 2016, 94, 042408.

37. B. Voigtlander, Scanning Probe Microscopy: Atomic Force Microscopy and Scanning Tunneling Microscopy (Springer-Verlag, Berlin, Heidelberg, New Nork, 2015).

38. Y. Martin, C. C. Williams, and H. K. Wickramasinghe, J. Appl. Phys, 1987, 61, 4723–4729.

39. S. N. Magonov, V. Elings, and M. H. Whangbo, Surf. Sci, 1997, 375, L385–L391.

40. N. G. Green and H. Morgan, J. Phys. Chem. B, 1999, 103, 41–50.

41. H. Imasato and T. Yamakawa, J. Electrophoresis, 2008, 52, 1–8.

CHAPTER 3. ELECTRONIC PROPERTIES OF NANOMATERIALS IN FIELD EFFECT TRANSISTORS

3.1. Introduction to Carbon Nanomaterials

Carbon nanotubes (CNTs) are hollow cylinders the walls of which are made of covalently bonded carbon atoms arranged in a honeycomb configuration (Figure 3.1). They can either form as a single tube called a single-walled CNT or as many concentric tubes called multi-walled CNTs. First discovered by Ijima in 1991 (1).

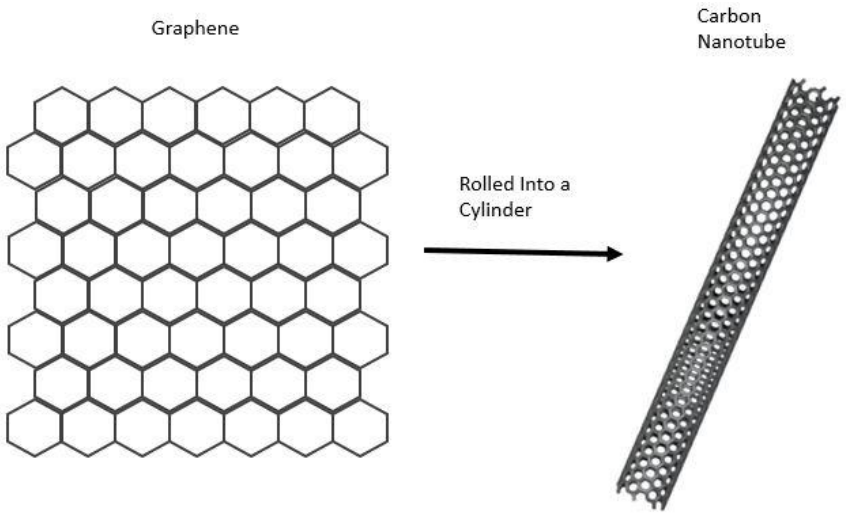

Fig. 3.1: A graphene sheet (left) consisting of a two-dimensional honeycomb lattice of carbon atoms. Rolling this structure into a tube forms a carbon nanotube (right).

However, the CNTs in this thesis were grown via chemical vapor deposition, a method that has become popular recently due to its ability to grow CNTs with fewer defects. In this technique, a carbon-containing gas is sent through a furnace ranging from 700-1000° C (2) across a substrate such as silicon oxide that has been patterned with a metal catalysts (commonly iron particles), causing carbon atoms to deposit onto the metal particles and form CNTs. A CNT can be either metallic or semiconducting depending on the chiral angle (the angle between the axis and the carbon lattice orientation).

Graphene, meanwhile, is a honeycombed carbon material similar to a single-walled CNT, but in the shape of a sheet instead of a tube (Figure 3.1). Due to their similarities, the band structure of graphene can be used to calculate the band structure of CNTs, and it is much easier than calculating the band structure of CNTs directly.

3.2. Theory Behind Electronic Properties

The real-space crystal of graphene is a single-atom thick lattice of carbon atoms in a honeycomb pattern, and has lattice vectors of $\overrightarrow{a_1} = (\frac{a\sqrt{3}}{2}, \frac{a}{2})$ and $\overrightarrow{a_2} = (\frac{a\sqrt{3}}{2}, -\frac{a}{2})$ and a lattice constant of $a = 2.46$ angstroms (Figure 2.2(a)). Graphene's reciprocal lattice is also a honeycomb lattice with reciprocal lattice vectors of $\overrightarrow{b_1} = (\frac{2\pi}{a\sqrt{3}}, \frac{2\pi}{a})$ and $\overrightarrow{b_2} = (\frac{2\pi}{a\sqrt{3}}, -\frac{2\pi}{a})$ (Figure 3.2(b)). The chiral vector of a CNT has the form of $\vec{C} = n\overrightarrow{a_1} + m\overrightarrow{a_2}$ (1) (Figure 3.2(c)) (3,4) and is the vector that goes between the points on the graphene carbon lattice that contact each other when the graphene sheet is rolled into the CNT. This vector defines the carbon atoms' orientations with respect to each other in a CNT, and controls whether or not the CNT is metallica or semiconducting, as will be shown later in this chapter.

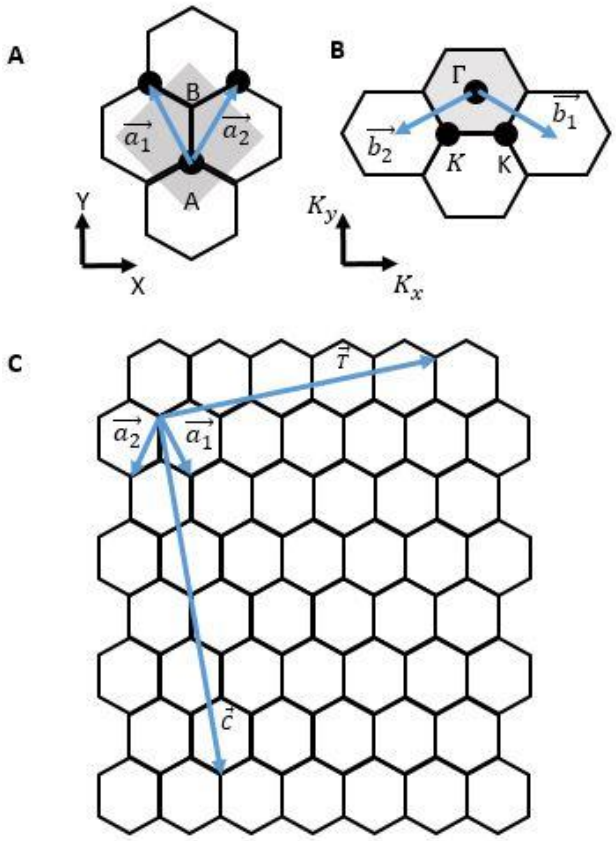

Fig. 3.2: (A) The lattice vectors $\overrightarrow{a_1} = (\frac{a\sqrt{3}}{2}, \frac{a}{2})$ and $\overrightarrow{a_2} = (\frac{a\sqrt{3}}{2}, -\frac{a}{2})$ on the real-space graphene lattice. The unit cell is shaded in grey. (B) The reciprocal space lattice vectors $\overrightarrow{b_1} = (\frac{2\pi}{a\sqrt{3}}, \frac{2\pi}{a})$ and $\overrightarrow{b_2} = (\frac{2\pi}{a\sqrt{3}}, -\frac{2\pi}{a})$ with the Brillouin zone shaded in grey. (C) By rolling the graphene strip into a cylinder, a carbon nanotube can be created. The vector $\vec{T}$ is points parallel to the carbon nanotube axis and is known as the translation vector. $\vec{C}$ is the chiral vector and points from the origin to the point that will contact the origin after the graphene sheet is rolled into a nanotube (4).

The band structure of graphene can be calculated using the tight-binding method as shown by (5) by calculating the eigen-values for the Hamiltonian related to the two carbon atoms making up the unit cell of the graphene. The Hamiltonian and overlap integral matrix for graphene has been shown to be (6):

$$H = \begin{pmatrix} E_{2p} & \Phi_k \\ \Phi *_k & E_{2p} \end{pmatrix}, S = \begin{pmatrix} 1 & \frac{s}{t}\Phi_k \\ \frac{s}{t}\Phi *_k & 1 \end{pmatrix} \quad (3.1)$$

where,

$$\Phi(k) = te^{ik_x\frac{a}{\sqrt{3}}}(1 + 2e^{-ik_x\frac{a\sqrt{3}}{2}}\cos\left(k_y\frac{a}{2}\right)) \quad (3.2)$$

This can be simplified further by only including the upper π^*band and the lower π band, this eliminating the need for the overlap integral matrix and setting $E_{2p} = 0$. The eigenvalues can then be solved by:

$$E(k) = \pm|\Phi(k)| \quad (3.3)$$

Therefore, the electronic band structure of graphene can be calculated:

$$E(k) = \pm t\sqrt{1 + 4cos^2\left(\frac{k_y a\sqrt{3}}{2}\right) + 4\cos\left(\frac{k_y a\sqrt{3}}{2}\right)\cos\left(\frac{3k_y a}{2}\right)} \quad (3.4)$$

By plotting this function it can be seen that graphene's band structure contains periodic cone-shapes at the K points (represented in Figure 3.3).

The band structure that results from this is abnormal in that the conductance and valence bands only touch at the K points and at those points, the energy changes approximately linearly with the wavevector, as can be seen in Figure 3.3. This leads to graphene being characterized as a zero-gap semiconductor, and allows graphene to be used in field-effect transistor technology which will be discussed later. By writing $\vec{k}$ with respect to K, the energy close to that point can be expressed as (3):

$$E(\vec{k}) \approx \pm(2.3\ eV)ka \quad (3.5)$$

Next, by applying the periodic boundary condition that exists when the graphene is rolled up, we get (3,7):

$$\vec{C} \cdot \vec{k} = 0,\ mod\ 2\pi \quad (3.6)$$

using $\vec{C}$ as the chiral vector. The one-dimensional band structure that results from this can be seen in Figure 3.3. The CNT band structure can be imagined as cross sections taken from the

graphene band structure, and is thus only metallic if the $\vec{k}$ vectors go through the K points, otherwise the CNT is semiconducting. In the metallic case, the $\vec{k}$ vector must meet the above boundary condition, thus:

$$\vec{C} \cdot \overrightarrow{k_K} = (n\overrightarrow{a_1}, m\overrightarrow{a_2}) \cdot \left(\frac{2\pi}{a\sqrt{3}}, \frac{2\pi}{3a}\right) = 2\pi\left(\frac{2}{3}n + \frac{1}{3}m\right) \tag{3.7}$$

By applying the periodic boundary condition:

$$2n + m = 0,\ mod\ 3 \tag{3.8}$$

Thus, one-third of CNTs are metallic, while two-thirds are semiconducting, if it is assumed that the likelihood of (n,m) combinations are the same. For the biosensing applications written about in this thesis, the exact band gap size is not as important as just the fact that many of the CNTs are semiconductors.

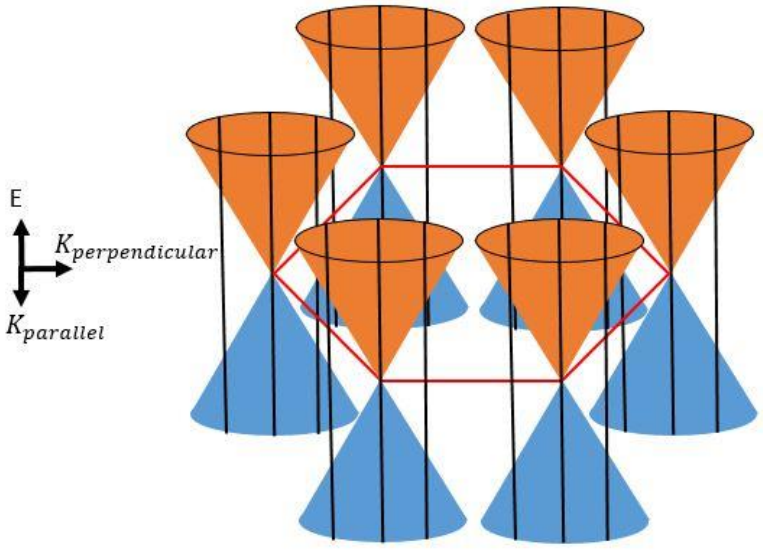

Fig. 3.3: The graphene band structure can be approximated as a system of cones near the Fermi energy. In the reciprocal lattice, at each K point, the conduction (orange) and valence (blue) bands touch. The electron states become quantized perpendicularly to the axis as the graphene sheet is rolled into a carbon nanotube (7), and the intersections of the graphene band structure and the allowed nanotube wavevectors dictate the carbon nanotube's allowed electron states (represented by the vertical black lines intersecting the cones) (3).

3.3. Carbon Nanotube Field Effect Transistors

Due to the fact that two-thirds of carbon nanotubes are semiconductors, they can be used to create field-effect transistors. This is done by fabricating two electrodes onto an insulating layer such as SiO_2 on top of a conducting layer, referred to as the back gate, often made from doped silicon. A single CNT is then connected between the two electrodes, called the source and drain, creating a channel between the two (Figure 3.4(a)).

From the semiconducting CNT band diagram (Figure 3.4(b)), it can be seen that the CNT is either conducting or turned off depending on whether or not the Fermi level is in the conductance band or the band gap, and this can be adjusted by changing the gate voltage. At low gate voltages, the band structure stays constant near the electrode-CNT contacts, due to the electrodes shielding the CNT from the electric field. However, far enough from the electrodes, the electric field bends the band structure upwards. The Fermi level in this case exists below the band gap so the device is conducting. At high gate voltages, the energy bands bend downwards, placing the Fermi level in the band gap and switching off the transistor (3). This can be seen in Figure 3.4.

Additionally, the CNT transistor can be made to conduct electrons instead of holes by raising the gate voltage until the Fermi level passes into the conductance band, allowing electrons to tunnel to the CNT conductance band from the contact valence band. However, this n-type of conduction leads to a smaller current than the previously discussed p-type conduction due to the tunnel barrier. In the research presented by this thesis, the CNTs are always used in the p-type mode and the CNTs are used to detect protein activity via charges on the protein surface.

Previously, we have proved that the SWNT-FET is extremely sensitive to electrostatic gating by the protein's charged residues within 1 nm of the attachment site (8). When a protein's

loop undergoes its opening and closing motions, the movement of these charges produces a time-varying electric fields that acts in addition to the constant, externally applied gating voltage V_G to produce a time-varying change in gating ΔV_G. Considering a set of protein charges q_i dynamically varying between positions $r_{i,1}$ and $r_{i,2}$, the consequence of these charges on the SWNT current will be,

$$\Delta I = \frac{\partial I}{\partial V_G}\Delta V_G \propto \frac{\partial I}{\partial V_G}\sum_i q_i \left(\frac{1}{r_{i,1}} - \frac{1}{r_{i,2}}\right) \exp\left(-r_{i,1}/\lambda_D\right) \tag{3.9}$$

where $\lambda_D$is the Debye screening length of the electrolyte. In this equation, the variability of ΔI(t) from one device to another is entirely due to the slope $\partial I/\partial V_G$, which is an empirical, device-dependent parameter. Otherwise, the q_i and r_i terms in the above equation are entirely determined by enzyme's structure and movements. These values are specific for each protein so it will be discussed in more detail in chapters 3 and 4 for the specific proteins being detected in those chapters.

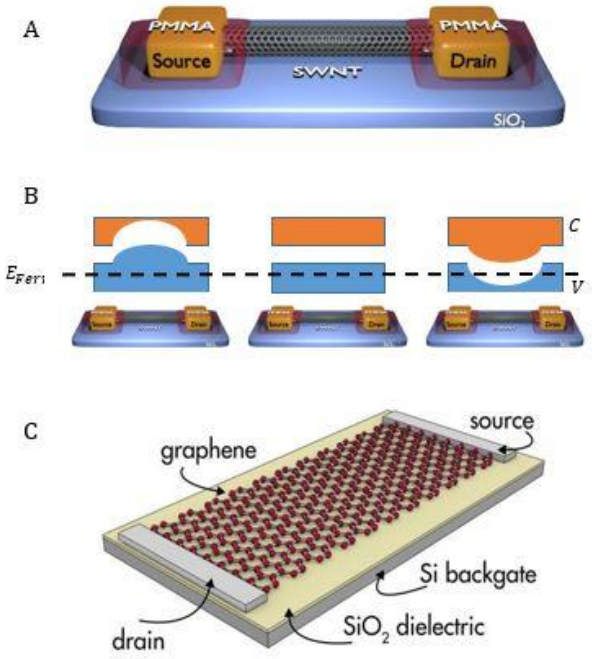

Fig. 3.4: (a) An example of a carbon nanotube transistor made of a source and drain electrode fabricated on an oxide layer on top of a conducting back gate. The two electrodes are connected with a single-walled, semiconducting carbon nanotube. (b) The band structure of the nanotube transistor at different voltage levels. The left image is the band structure at a low gate voltage, showing the band structure bend upwards along the nanotube as electrodes are displaced away from the nanotube towards the contacts. In this case the Fermi level is deep in the valence band (blue) so the device easily conducts p-type carriers. The middle image is the band structure at 0 V. In this case, the band structure bends back to neutral as no voltage is applied. The Fermi level is still in the valence band, so the device conducts holes but not as strongly as it did at a low gate voltage. In the right image, the band structure is bent downwards due to electrons being drawn onto the nanotube by the high gate voltage, and placing the Fermi level in the band gap, shutting off the device. (5) (c) Diagram of graphene FET, similar to the nanotube FET, but with a strip of graphene acting as the carrier channel in place of the nanotube.

3.4. Graphene Field Effect Transistors

Similar to most CNTs, graphene is also semiconducting, which means it can also be used to construct a field-effect transistor. However, due to graphene not having a band gap, the current will never be completely shut off, which prevents graphene transistors from being used in computing applications, but they can still be used as sensors. With this purpose, graphene transistors may be constructed in a similar way as the CNT transistors. Two electrodes are

fabricated on a conducting layer on top of a conducting back gate, and then a single layer of graphene is used to connect the two electrodes (Figure 3.4(c)).

Graphene transistors are also gated similarly to CNT transistors. By decreasing the gate voltage, the band structure across the graphene channel is pushed upwards and the Fermi level goes deeper into the valence band. As the gate voltage is increased, the band structure is lowered across the channel and the Fermi level moves closer to the K point where the valence and conductance bands meet. As it nears this point, the conductance across the graphene will decrease until the Fermi level is at the K point. At this point the conductance is at its lowest, and then as the gate voltage continues to increase, the Fermi level will be pushed into the conductance band, and the conductance will increase again as the graphene begins to conduct n-type carriers instead of p-type carriers. The differences between this behavior and the CNT transistor behavior is that in the case of the CNT there is a band gap, so there is a gate voltage at which the conductance of the CNT shuts off. Meanwhile, the graphene devices do not have band gaps, so although the conductance does reach a low point when the Fermi level is at the K point, it never actually goes to zero. Additionally, since there is no band gap, it is much easier to observe n-type conductance in the graphene transistors than the CNT ones since less gate voltage is required to push the Fermi level into the conductance band.

For sensing purposes, the graphene's conductance is affected by the target particles surface charges which apply an electric field onto the graphene surface, effectively altering the band structure at the point of contact. The exact nature of this interaction depends on the particle being detected. In this thesis, graphene transistors are used to detect exosomes originated from pancreatic cancer tumors. Therefore, this interaction will be explored in greater detail in chapter 5.

3.5. References

1. S. Iijima. Helical microtubules of graphitic carbon. Nature, 1991, 354:56.
2. J. Kong, A. M. Cassell, and H. Dai, . Chem. Phys. Lett, 1998, 292, 567.
3. L. Ouellette. Chemical and Biological Sensing with Carbon Nanotubes in Solution. PhD Thesis, Cornell University, 2008.
4. R. Saito, G. Dresselhaus, and M. S. Dresselhaus. Physical Properties of Carbon Nanotubes. Imperial College Press, London, 1998.
5. P. R. Wallace. Phys. Rev., 71:622, 1947.M.-T. Wei, J. Junio, and H. D. Ou-Yang, Biomicrofluidics, 2009, 3, 012003.
6. R. Saito, G. Dresselhaus, and M. S. Dresselhaus, Physical Properties of Carbon Nanotubes, Imperial, London, 1998.
7. T. W. Odom, J-L. Huang, P. Kim, C. M. Lieber, J. Phys. Chem. B, 2000, 104, 2794-2809.
8. Y. Choi, T. J. Olsen, P. C. Sims, I. S. Moody, B. L. Corso, M. N. Dang, G. A. Weiss and P. G. Collins, Nano Lett., 2013, 13, 625-631.

CHAPTER 4. REAL-TIME TRACKING OF SINGLE-MOLECULE COLLAGENASE ON THE NATIVE COLLAGEN AND PARTIALLY-STRUCTURED COLLAGEN-MIMIC SUBSTRATES[2]

4.1. MMP-Collagen Introduction

4.1.1. Importance of MMP-Collagen Studies

About 90% of deaths due to cancer involve tumors that metastasize to spread around the body (1,2). During proliferation, cancer cells overexpress and up-regulate matrix metalloproteinases (MMPs), which play a pivotal role in the degradation of almost all proteins of the extracellular matrix (ECM) (3). Although MMPs are closely involved in multiple human cancers, the MMPs' proteolytic activities with the collagen, a major element of ECM and the most abundant in human tissue, remain incompletely understood (4, 5).

The triggered release of drugs from liposomes has been recognized as a promising cancer therapeutic approach, in which the liposomes release their contents when the membranes are destabilized by an external trigger such as enzymes or pH (6, 7). For example, MMP-targeting liposomes synthesized by a triple-helical collagen-mimic lipopeptide have demonstrated the release of the anti-cancer contents triggered by MMPs at the target tumor site and the reduction of tumor size by the contents (6, 8, 9).

The enzymatic degradation of such liposomes depends on the triple-helical structure and cleavage site of the lipopeptides (8, 10). The increased helical conformation of the lipopeptides enhances thermal and structural stability, while the helicity decreases the catalytic efficiency of

[2] The material in this chapter was co-authored by James Froberg, W. Choi, A. Seddigh, T. Anajafi, J. Farmakes, Z. Yang, S. Mallik, D. K. Srivastava, and Yongki Choi. James Froberg was primarily responsible for experimental design, collecting data, analyzing data and drawing conclusions from the results.

MMPs to cleave and process the substrates, with a much more pronounced effect for MMP1 (8, 11). Thus, it is critical to develop novel lipopeptides that can provide structural and thermal stability to form three-dimensional liposomes with high susceptibility to MMP1 for the effective degradation.

Here, we synthesized the non-triple-helical, partially-structured collagen-mimic lipopeptides that include stearic acid and two GPO repeating units ($[CH_3(CH_2)_{16}CONHGPQGIAGQR(GPO)_2GG$; O represents 4-(R)-hydroxyproline], Fig. 4.1), in which the conjugation of stearic acid gives rise to the structural stability and the reduced helicity provides high susceptibility for degradation by MMP1. Neither GPO-free lipopeptides nor lipopeptides with multiple GPO repeats (n > 3) produce stable, non-triple-helically cross-linked structures (6, 8). Thus, the lipopeptides serves as an ideal analog substrate to examine the relationship between the enzyme kinetics and minor variation of substrate's structure.

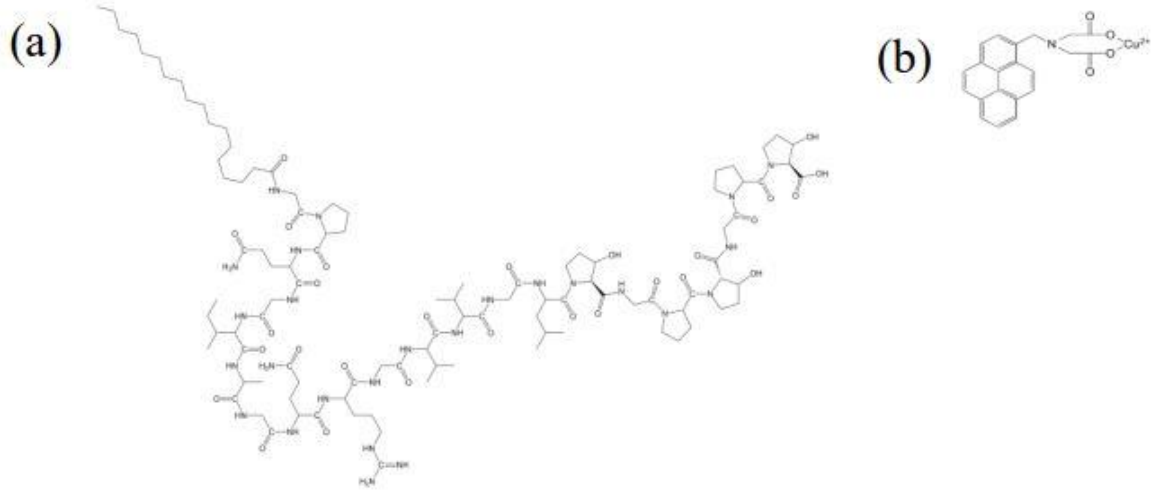

Fig. 4.1: Chemical structures of (a) a lipopeptide and (b) a pyrene-IDA-Cu2+ linker.

4.1.2. Importance of Our Single-Molecule Techniques

However, investigating dynamic interactions between individual MMPs and substrates is difficult using conventional fluorescence-based techniques for two main reasons. First, temporal,

spatial, and population averaging effects prevent probing of individual biological events (12) with substrates which could be heterogeneous in size and feature a cross-linked structure involving bindings of GPO repeats and fatty acids (6, 10). Second, signals from the optical techniques are limited by the complete dissociation of fluorophore-quencher units in the substrates regardless of their helicity, which not only preclude the observation of single cleavage events occurring each single-strand, but also interfere with enzymes' specificity and processivity. (13-15)

To overcome these issues, two complementary single-molecule techniques are applied here. We performed atomic force microscopy (AFM) measurements and electronic-based single-molecule nanocircuit measurements (16-18). Our measurements compare MMP1's catalytic ability, efficiency, processivity, and rate-limiting factors for the native collagen and lipopeptides substrates at a single-molecule level. The results provide detailed information about enzyme-ligand interaction at single-molecule resolution, providing new insights into designing effective drug carriers for enzyme-triggered contents-release.

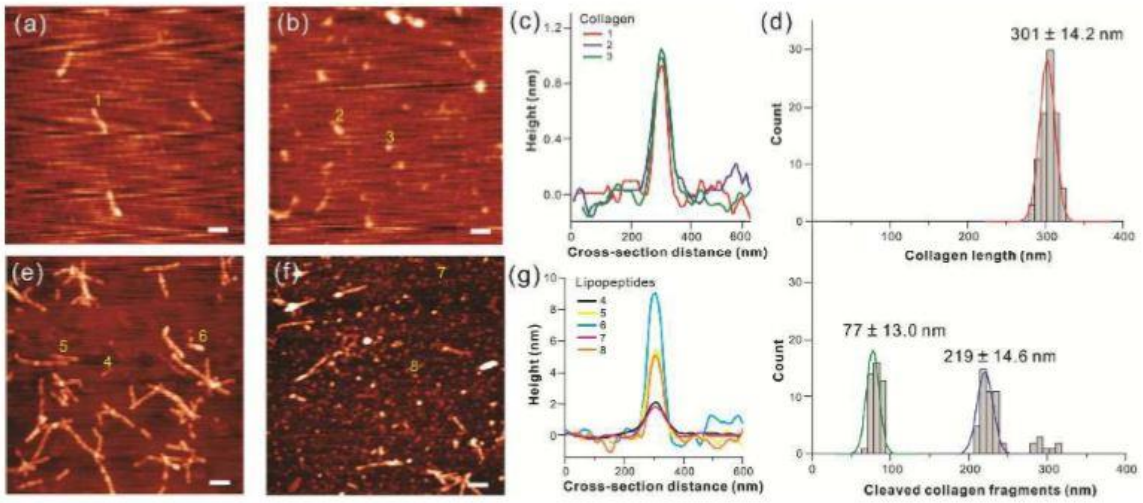

Fig. 4.2: AFM topography of collagen substrates before and after incubating with MMP1. (a) Single, triple-helical collagen molecules. (b) Cleaved collagen fragments after incubating MMP1. (c) Height profiles of collagen molecules extracted from the cross-sectional distance perpendicular to the molecules in (a) and (b). (d) Length distribution of collagen molecules before (top) and after (bottom) incubating with MMP1. (e) Non-triple-helical, partially-structured lipopeptides. (f) Cleaved lipopeptides after incubating with MMP1. (g) Height profiles of the lipopeptides in (e) and (f). All scale bars are 200 nm.

4.2. Results of MMP-Substrate AFM Experiments

4.2.1. Collagen Images Before and After Cleavage

Initially, the catalytic activities of MMP1 to both collagen and lipopeptides were investigated through AFM measurements (Fig. 4.2). Figures 4.2(a-d) demonstrate typical shape and dimension of the native, triple-helical collagen monomers before and after incubating with MMP1 for an hour in an assaying buffer (100 mM Tris-HCl, pH 7.5, 10 mM $CaCl_2$, 100 mM $NaCl_2$). The AFM images clearly show individual collagen monomers with an average length of 301 nm and height of 1 nm. After incubating with MMP1, collagen fragments in length, compared to the intact collagen monomers, appeared in the AFM image. Figure 4.2(d) compares the overall length distributions of the intact collagen and cleaved collagen fragments, splitting from a single peak at 301 nm to two peaks at 77 nm and 219 nm with no changes of their heights. These observations reflect the hydrolysis of the specific amide bond between G and I in the

collagen molecule by MMP1, creating two collagen fragments, one ¼ and the other ¾, which are consistent with previous AFM studies (19-21).

4.2.2. Lipopeptide Images Before and After Cleavage

Similar to the native collagen, the lipopeptides were prepared and imaged by the AFM under the same conditions (Figs. 4.2(e-g)). The AFM images show the lipopeptides in rodlike shapes with various lengths, heights (2-10 nm) and crosslinks (Fig. 4.2(e)). After incubating the lipopeptides with MMP1 for an hour, the AFM images revealed many short fragments in both lengths and heights, indicating almost complete digestion of the lipopeptides by MMP1 (Fig. 4.2(f)).

The increased height and various lengths of the lipopeptides suggest that the lipopeptides form bundles of single lipopeptides. However, the lipopeptides do not have the minimum number of GPO repeats, which twist to form a triple-helical conformation and a collagen fibril with the native collagen. Thus, both the hydrophobic interactions between fatty acids at one end and the weak interaction between two GPO repeats at the other end could contribute to the formation of bundles in non-helical, linear conformation, producing the rod-like lipopeptides. Also, non-specific interaction between the lipopeptides and bundles provide additional freedom to branch out, cross-link, and stack each other randomly, yielding various heights in AFM images.

Although the lipopeptides are bundled up and partially structured with many single lipopeptides, almost all bundles and cross-links were cleaved by the MMP1, indicating the high susceptibility to MMP1. These observations in AFM measurements proved the preserved proteolytic activity of MMP1 with both substrates regardless of triple-helicity and crosslinked structures.

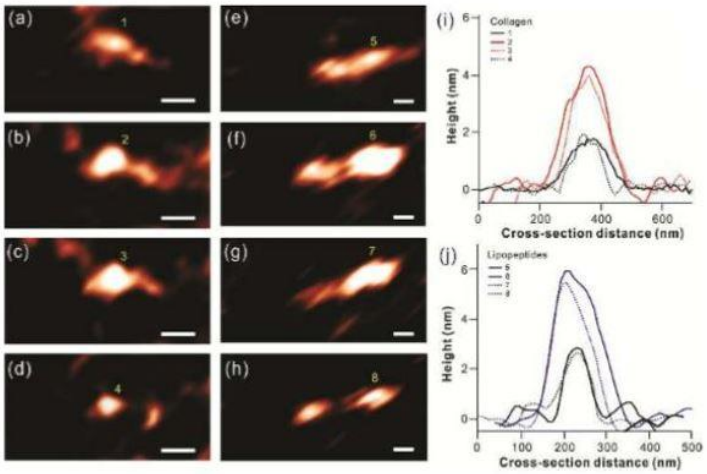

Fig. 4.3: Real-time interactions between an individual MMP1 and a substrate. Time-series AFM images of (a)-(d) the collagen molecule and (e)-(h) the lipopeptide after perfusion of MMP1. The images were recorded at 8 min. and 6 min. intervals for the collagen and lipopeptide, respectively. All scale bars are 100 nm. Height profiles of (i) the collagen and (j) lipopeptide are included as well.

4.3. Results of MMP-Substrate Real-Time AFM Experiments

The real-time interactions between individual MMP1 and both substrates were monitored using liquid-AFM imaging in the buffer solution (Fig. 4.3). Figures 4.3(a-d) depict time-series AFM measurements of the binding and cleavage of the individual collagen molecule by MMP1.

Initially, the AFM probe scanned over the collagen and identifies single collagen monomers (Fig. 4.3(a)). Following the addition of MMP1 (6 μM), the AFM probe re-scanned the same collagen monomer, capturing a MMP1 attachment to the monomer and formation of a MMP1-collagen complex (Fig. 4.3(b)). Next, subtle conformational changes of the complex were observed while continuously monitoring the complex, suggesting either unwinding of the triple-helical collagen or the hydrolysis of the amide bond (Fig. 4.3(c)). During these processes, we observed the increase in height after MMP1 binding to the collagen (Figs. 4.3(a-b), 4.3(i)), as well as the slight decrease in height due to subtle conformational changes of the complex (Figs. 4.3(b-c), 4.3(i)). After cleavage, the MMP1 diffused away from the complex, leaving two short

collagen fragments (Fig. 4.3(d)). A similar interaction between an individual MMP1 and lipopeptide was monitored and recorded (Figs. 4.3(e-h)). Figures 4.3(i-j) present the height profiles of the substrates and complex, which were consistent before and after cleavage and with the AFM measurements performed in dry conditions (Fig. 4.2).

The AFM images in Fig. 4.3 visualize real-time intermolecular interaction between MMP1 and collagen substrates at single-molecule resolution. MMP1 formed the MMP-substrate complex at an off-center position of the substrates and then dissociated from the same position, leaving two short fragments. Previous work has demonstrated that MMP8 is able to nonspecifically bind non-cleavage sites of collagen monomers, but unable to cleave (19) and that MMP1 randomly binds and diffuses along the collagen fibrils to find the cleavage sites (22). When MMP1 recognizes and bind the cleavage sites, cleavage takes place as demonstrated in our real-time AFM measurements. We note that the slow catalytic activity observed here could result from the surface effect, which limits diffusion of both MMP1 and collagen and interferes with conformational motions of MMP1 while binding, unwinding, and catalyzing the surface-bound collagen.

4.4. Results of MMP-Substrate Real-Time Nano-Circuit Experiments

4.4.1. Nano-Circuit Set-Up

To further investigate the kinetics during the catalysis and complement the real-time AFM observations, we performed single-molecule nano-circuit measurements, which provide excellent temporal resolution (< 20 μs) and long period time (>20 min) measurements. For MMP1-nanocircuits, individual MMP1 molecules were attached to the sidewalls of single-walled carbon nanotube (SWNT) field-effect transistors (FETs) (Depicted in Figure 4.4) through the pyrene-iminodiacetate-Cu^{2+} linker molecules (Fig. 4.1), in which the Cu^{2+} ion binds to N-

terminal His-tag of MMP1 and the pyrene moiety binds to the sidewall of the SWNT through π-π interaction (16, 18). Thus, MMP1 can freely interact with substrates and form the MMP1-substrate complex. When MMP1 or the complex undergoes conformational changes to bind, unwind, hydrolyze, and release the products, motions of charge residues associated with the conformational transition induce current fluctuations (ΔI(t)) underlying the SWNT-FET through a charge gating effect that has been proven by our previous work (17, 18). Therefore, the MMP1-nanocircuits directly record MMP1's dynamic conformational changes as it degrades its substrates.

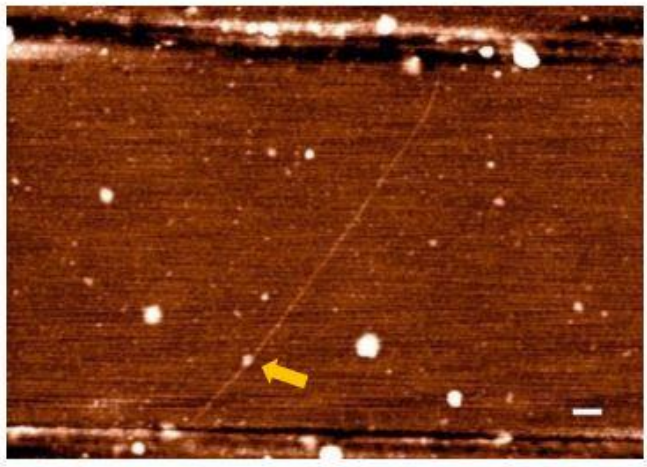

Fig. 4.4: Example AFM topography of SWNT-FET device with a single MMP attachment (arrow). Scale bar is 200 nm.

4.4.2. Nano-Circuit Measurement Results

Figure 4.5 depicts typical ΔI(t) signals measured with the nanocircuit under different conditions. In the absence of the substrates as control measurements, ΔI(t) signals exhibited no meaningful features which serve as a baseline current (Fig. 4.5(a)). Following the addition of collagen monomers (1 μg/ml) to the MMP1-nanocircuit, several current spikes above the baseline current were captured (Fig. 4.5(b)). Such current spikes maintained for a short period time (~few ms) with a magnitude of ~6 nA (Fig. 4.5(b) inset). Figure 4.5(c) illustrates the similar

ΔI(t) fluctuations between two current states, but substantially increased number of spikes when the lipopeptides were added to the same MMP1-nanocircuit.

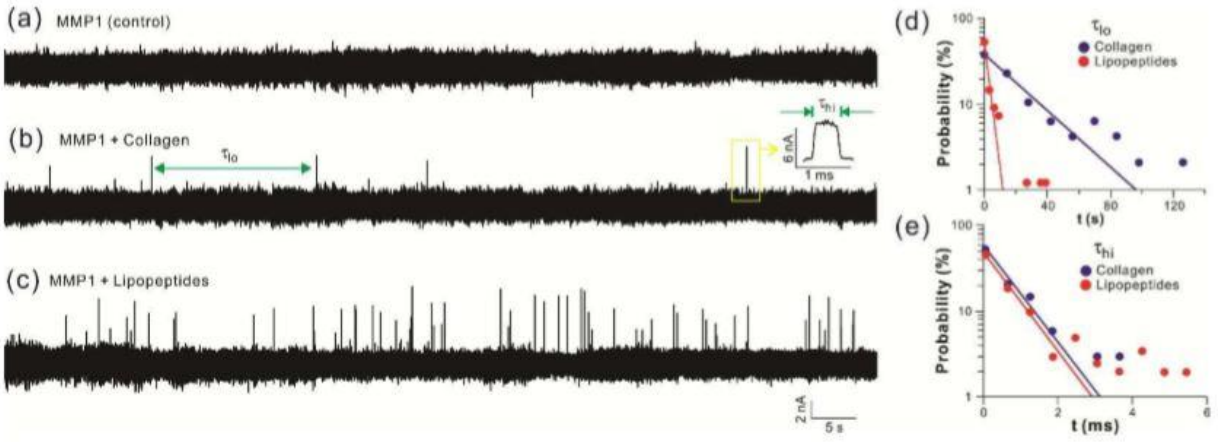

Fig. 4.5: Electronic current ΔI(t) fluctuations of the MMP1-nanocircuit. (a) In the absence of substrates (buffer only), no current fluctuations were observed. The addition of (b) the collagen and (c) lipopeptides resulted in the current spikes, fluctuating between the low and high current states, which corresponds to the enzymatic turnover events. Comparison of probability distributions of (d) the low state (τ_{lo}) and (e) high state (τ_{hi}) for both substrates. Single exponential fits are shown as solid lines, determining the mean value of τ .

Crystallographic and computational studies have identified that the active site pocket of MMP1 is initially narrow (closed conformation, diameter of ~5 Å), which allows triple-helical collagen molecules to bind to MMP1's pocket surface, but hinders triple-helical conformation (diameter of ~15 Å) from entering into the catalytic zinc atom located inside of the pocket ~7 Å away from the entrance surface (23, 24). Following unwinding of the triple-helix, the single strand could enter into the catalytic site to be cleaved by two fragments (24, 25). Next, the pocket opens (open conformation) to remove the cleaved fragments and closes it for adoption and hydrolysis of following strands (24). During such conformational rearrangement, motions of charged side chains of Arg108 and Glu110 in proximity to SWNT binding sites (the N-terminus) electrostatically gate the SWNT channel current, resulting in two distinguishable current states (26, 27). Thus, we assign the low and high current states of the signals to correspond to closed and open conformation of the MMP1 (Fig. 4.6).

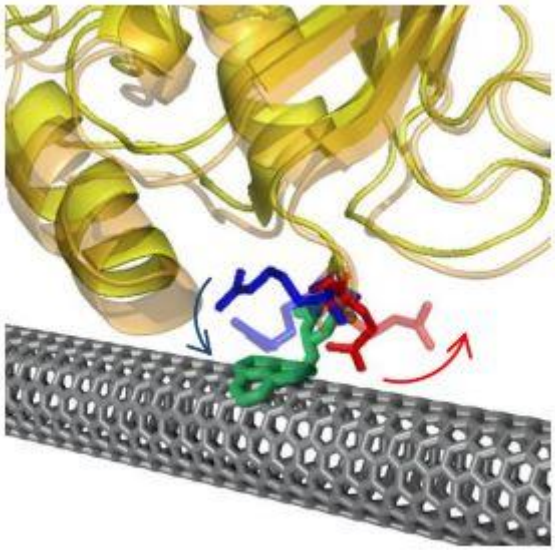

Fig. 4.6: Detailed view of the MMP1-SWNT interface, showing crystal structures of the MMP1 in its closed and open conformations

Therefore, the individual spikes in Figs. 4.5(b-c) represent conformational transitions of MMP1 associated with the catalytic processing of the substrates. The hydrolysis of the triple-helical collagen is known to be a very slow process due to the unwinding of the triple-helix before cleavage events, (14, 28) resulting in only a few spikes during the measurements. However, the catalytic activity of MMP1 with the lipopeptides has substantially increased, proving that MMP1 does not require triple-helical conformations, nor is it hindered by the cross-links of the fatty acid or GPO repeats for its processivity.

Figures 4.5(d-e) show the probability distribution of the duration in the low (τ_{lo}) and high (τ_{hi}) current states accumulated from more than 600 s of recordings. The distributions fit an exponential, suggesting a single mean value of τ. In the presence of the native collagen substrate, the mean τ_{lo} and τ_{hi} were measured to be 26 s and 0.78 ms, respectively (Figs. 4.5(d-e), blue color). With the lipopeptides, the mean τ_{lo} (2.9 s) was decreased by a factor of 10, but no significant changes in the mean τ_{hi} (0.74 ms) (Figs. 4.5(d-e), red color). The overall turnover rate, $1/(\tau_{lo} + \tau_{hi})$, also increased almost tenfold due to the major contribution of τlo to the rate.

While unusually long durations for each state at the distribution tail are slightly off from the fit, occurrence of such events are extremely rare (< 5%), and thus no significant contribution to the mean duration τ. The mean τ values, turnover rates, variance analysis, and relative energy differences of each substrate are summarized in Table 4.1.

4.4.3. MMP1 Turnover Rates

The rate k=0.038 s^{-1} of MMP1 with the collagen monomers are in agreement with the kcat from previous bulk measurements (28, 29). Thus, the current fluctuations correspond to enzymatic turnover events. The increased rate of k=0.345 s^{-1} with the lipopeptides suggest more catalytic events occurring by MMP1. Since the lipopeptides do not have triple-helical structures, MMP1 could cleave them without the intermediate step of unwinding the helical conformation.

Table 4.1: Single Molecule Kinetic Parameters

Substrates	τ_{lo}(s)	r_{lo}	τ_{hi}(ms)	r_{hi}	Rate (1/s)	ΔE (kcal/mol)
Collagen	26 ∓ 1.8	0.49 ∓ 0.34	0.78 ∓ 0.04	0.98 ∓ 0.44	0.038	6.25
Lipopeptide	2.9 ∓ 0.26	0.71 ∓ 0.32	0.74 ∓ 0.05	1.00 ∓ 0.26	0.345	4.96

This effective catalytic pathway resulted in the significant reduction of duration in the closed conformation (88 %), implying that the unwinding step could be the major rate-limiting step during the entire catalytic cycle.

To further assess the number of rate-limiting steps in the reaction pathway, the mean normalized variance r=σ_2/τ_2 of the τ_{lo} and τ_{hi} is used (30). For the collagen, the variance r_{lo}=0.71 (= 1/n, n is the number of the rate limiting steps) suggests that the conformational transition from closed to open involves at least two steps, but non-identical, rates. In contrast, the variance r_{lo}≈1 for the lipopeptides indicates the duration of the conformational transition is rate-limited by a single-step Poisson process. Taken together, we conclude that one of the major rate-

liming steps in the closed conformation is the unwinding of the triple-helical conformation before cleavage, which disappeared during substantially reduced τ_{lo} with the non-triple helical lipopeptides.

Despite the major differences in τ_{lo} and r_{lo}, the mean τ_{hi}=0.74-0.78 ms and the variance r_{lo}=0.98-1.00 were almost identical for both substrates. These results indicate that the open conformation lasts briefly to release the cleaved fragments from the active site pocket, which is the only rate-limiting step for the conformational transition from open to close to process a following non-helical collagen strand. In other words, the kinetics and rates from the hydrolysis to products release remain remarkably identical for both substrates. Although the structural stability of the lipopeptides and its contribution to the catalytic efficiency have not been identified in the present report, we could conclude that MMP1 can efficiently catalyze the lipopeptides compared to the structurally-stable, triple-helical collagen substrates.

Finally, the thermodynamic energy differences ΔE between the two current states, corresponding to the ratio of τ_{lo} and τ_{hi}, were investigated. In MMP1, the open conformation is much shorter than the closed conformation, indicating that this conformation requires higher energy to access. Using Boltzmann statistics, this energy difference can be calculated as $\Delta E = kBT\ln(\tau_{hi}/\tau_{lo})$ (31). ΔE were measured to be 6.25 kcal/mol and 4.96 kcal/mol for the collagen and lipopeptides, respectively. The reduction of 1.29 kcal/mol between triple-helical and single-strand conformation can probably be interpreted as the extra energy required for the unwinding of the triple-helix. Although the energy barrier was reduced by ~20 %, the overall catalytic turnover of MMP1 resulted in a drastic increase by a factor of 10. Furthermore, Δ E values were obtained when either substrate is bound to the MMP1. In the absence of either

substrate, no two-state ΔI(t) signal was observed, indicating that the open conformation is inaccessibly higher in energy associated with dissociation of the products.

4.5. Summary of MMP-Substrate Experiments

In conclusion, our AFM measurements demonstrated the real-time cleavage of the triple-helical collagen and non-triple-helical, partially-structured lipopeptide substrates by MMP1 at single-molecule resolution. From nanocircuit measurements, we observed that the kinetic rates and rate-limiting steps were highly sensitive to the substrate's structure, resulting in tenfold increased catalysis with lipopeptides. These results provide a detailed look of kinetics during the overall MMP1-ligand reaction, helping design new lipopeptides for MMP-targeting, drug-containing liposomes.

4.6. References

1. P. Mehlen and A. Puisieux, Nat. Rev. Cancer, 2006, 6, 449.
2. M. M. Taketo, Cancer Prev. Res., 2011, 4, 324–328.
3. A. Page-McCaw, A. J. Ewald and Z. Werb, Nat. Rev. Mol. Cell Biol., 2007, 8, 221–233.
4. P. F. Lu, V. M. Weaver and Z. Werb, J. Cell Biol., 2012, 196, 395–406.
5. M. Egeblad and Z. Werb, Nat. Rev. Cancer, 2002, 2, 161–174.
6. A. I. Elegbede, J. Banerjee, A. J. Hanson, S. Tobwala, B. Ganguli, R. Wang, X. Lu, D. K. Srivastava and S. Mallik, J. Am. Chem. Soc., 2008, 130, 10633–10642.
7. A. A. Kale and V. P. Torchilin, J. Liposome Res., 2007, 17, 197–203.
8. J. Banerjee, A. J. Hanson, B. Gadam, A. I. Elegbede, S. Tobwala, B. Ganguly, A. V. Wagh, W. W. Muhonen, B. Law, J. B. Shabb, D. K. Srivastava and S. Mallik, Bioconjugate Chem., 2009, 20, 1332–1339.

9. J. Banerjee, A. J. Hanson, E. K. Nyren-Erickson, B. Ganguli, A. Wagh, W. W. Muhonen, B. Law, J. B. Shabb, D. K. Srivastava and S. Mallik, Chem. Commun., 2010, 46, 3209–3211.

10. M. D. Shoulders and R. T. Raines, Annu. Rev. Biochem., 2009, 78, 929–958.

11. D. Minond, J. L. Lauer-Fields, H. Nagase and G. B. Fields, Biochemistry, 2004, 43, 11474–11481.

12. H. P. Lu, Curr. Pharm. Biotechnol., 2009, 10, 522–531.

13. J. L. Lauer-Fields, K. A. Tuzinski, K.-I. Shimokawa, H. Nagase and G. B. Fields, J. Biol. Chem., 2000, 275, 13282–13290.

14. J. L. Lauer-Fields, T. Broder, T. Sritharan, L. Chung, H. Nagase and G. B. Fields, Biochemistry, 2001, 40, 5795–5803.

15. T. K. Robichaud, B. Steffensen and G. B. Fields, J. Biol. Chem., 2011, 286, 37535–37542.

16. S. You, J. Froberg, J. Yu, M. Haldar, A. Sedigh, S. Mallik, D. K. Srivastava and Y. Choi, Chem. Commun., 2017, 53, 3307–3310.

17. Y. Choi, T. J. Olsen, P. C. Sims, I. S. Moody, B. L. Corso, M. N. Dang, G. A. Weiss and P. G. Collins, Nano Lett., 2013, 13, 625–631.

18. Y. Choi, I. S. Moody, P. C. Sims, S. R. Hunt, B. L. Corso, G. A. Weiss and P. G. Collins, Science, 2012, 335, 319–324.

19. H. B. Sun, G. N. Smith, K. A. Hasty and H. Yokota, Anal. Biochem., 2000, 283, 153–158.

20. L. Bozec and M. Horton, Biophys. J., 2005, 88, 4223–4231.

21. G. Rosenblum, P. E. Van den Steen, S. R. Cohen, A. Bitler, D. D. Brand, G. Opdenakker and I. Sagi, PLoS One, 2010, 5, e11043.

22. Susanta K. Sarkar, B. Marmer, G. Goldberg and Keir C. Neuman, Curr. Biol., 2012, 22, 1047–1056.

23. L. Chung, K.-i. Shimokawa, D. Dinakarpandian, F. Grams, G. B. Fields and H. Nagase, J. Biol. Chem., 2000, 275, 29610–29617.

24. B. Ivano, C. Vito, F. Marco, L. Claudio, M. Massimiliano and Y. K. Joo, Angew. Chem., Int. Ed., 2006, 45, 7952–7955.

25. J. Bella, M. Eaton, B. Brodsky and H. Berman, Science, 1994, 266, 75–81.

26. J. Li, P. Brick, M. C. O'Hare, T. Skarzynski, L. F. Lloyd, V. A. Curry, I. M. Clark, H. F. Bigg, B. L. Hazleman, T. E. Cawston and D. M. Blow, Structure, 1995, 3, 541–549.

27. B. Ivano, C. Vito, C. Linda, F. Marco, G. F. G. C. Carlos, H. Petr, L. Claudio, P. Giacomo and T. M. C. Joa˜o, FEBS Lett., 2012, 586, 557–567.

28. H. G. Welgus, J. J. Jeffrey and A. Z. Eisen, J. Biol. Chem., 1981, 256, 9511–9515.

29. E. Ohuchi, K. Imai, Y. Fujii, H. Sato, M. Seiki and Y. Okada, J. Biol. Chem., 1997, 272, 2446–2451.

30. W. Min, B. P. English, G. Luo, B. J. Cherayil, S. C. Kou and X. S. Xie, Acc. Chem. Res., 2005, 38, 923–931.

31. S. N. Xie, Single Mol., 2001, 2, 229–236.

CHAPTER 5. REAL-TIME MONITORING OF CONFORMATIONAL TRANSITIONS OF SINGLE-MOLECULE HISTONE DEACETYLASE WITH NANOCIRCUITS[3]

5.1. Introduction to the Monitoring of Histone Deacetylase 8 Kinetics

5.1.1. Importance of HDAC8 Studies

The dynamics of protein conformation play a major role during protein–protein and protein–ligand interactions, but remain a central question with enormous importance for the design of drugs (1-5). For example, multiple conformational subset states of proteins result in significant differences in their affinity, selectivity, and reactivity (7). Thus, it is critical to understand the protein dynamics and their roles in ligand recognition, catalysis, and inhibition to advance the relevant design of pharmacologically efficient anti-disease drugs.

Recently, histone deacetylase 8 (HDAC8) has gained considerable attention regarding the design of drugs for a variety of human diseases due to its involvement in epigenetic regulation (7-10). The enzyme catalyzes the hydrolysis of acetyl-lysine residues in histone proteins to promote gene repression and silencing. X-ray crystallography and nuclear magnetic resonance studies have revealed that HDAC8 is a highly flexible enzyme, undergoing 5–10 Å conformational rearrangements to adopt and catalyze differently-structured ligands (11-13). In addition, several conformational subset states of a HDAC8–ligand complex and an interconversion between the states have been observed in computational modeling studies (14). However, direct measurements of such dynamic features have not been achieved due to the

[3] The material in this chapter was co-authored by Seungyong You, James Froberg, J. Yu, M. Haldar, A. Seddigh, S. Mallik, and Yongki Choi. James Froberg and Seungyong You worked together and were primarily responsible for experimental design, collecting data, analyzing data and drawing conclusions from the results.

averaging effects from ensemble-assay measurements and the limited dynamic information from crystallographic methods.

5.1.2. Single Molecule Approach

Here, we apply a novel, electronic single-molecule approach to examine the real-time dynamics of the HDAC8–ligand complex over long periods of time, which are usually limited in single molecule fluorescence resonance energy transfer measurements due to fluorophore bleaching (15-16). To systematically monitor the dynamic interaction between HDAC8 and ligands, two configurations of nanocircuits are prepared (Fig. 5.1). First, we synthesized pyrene-suberoylanilide hydroxamic acid (pSAHA) inhibitors ((Fig. 5.2) to attach to the sidewalls of single-walled carbon nanotube (SWNT) field-effect transistors (FETs) (Fig. 5.1(a), pSAHA-nanocircuits). The aromatic pyrene moiety adheres to the SWNT sidewall *via* π–π interactions and the SAHA-inhibitor interacts with freely-diffusive HDAC8 enzymes to form a HDAC8–pSAHA complex.

As the complex undergoes conformational changes, motions of charge residues associated with the conformational changes induce current fluctuations underlying the SWNT-FET through a charge gating effect, which have been clearly demonstrated in our previous work (17,18). Second, individual HDAC8 molecules attached to the SWNT-FETs (Fig. 5.1(b), HDAC8-nanocircuits) using pyrene-iminodiacetate (IDA)-Cu^{2+} linker molecules (Fig. 5.2 in which Cu^{2+} ions bind to the N-terminal His-tag of HDAC8. The dynamic motions of the HDAC8–ligand complex formed with freely-diffusive ligands including coumarin-SAHA (Fig. 5.2 cSAHA), a potent *N*(phenylcarbothiol)benzamide activator (19) (Fig. 5.1(c), hereafter ACT), and a trifluoroacetyl-lysine-methylcoumarin conjugate substrate (Fig. 5.2 TFAL-AMC) also induce fluctuations in the SWNT-FET current through a similar gating effect. An atomic force

microscopy (AFM) image (Fig. 5.1(d)) confirmed the presence of a single attached HDAC8 on the SWNT-FET nanocircuits.

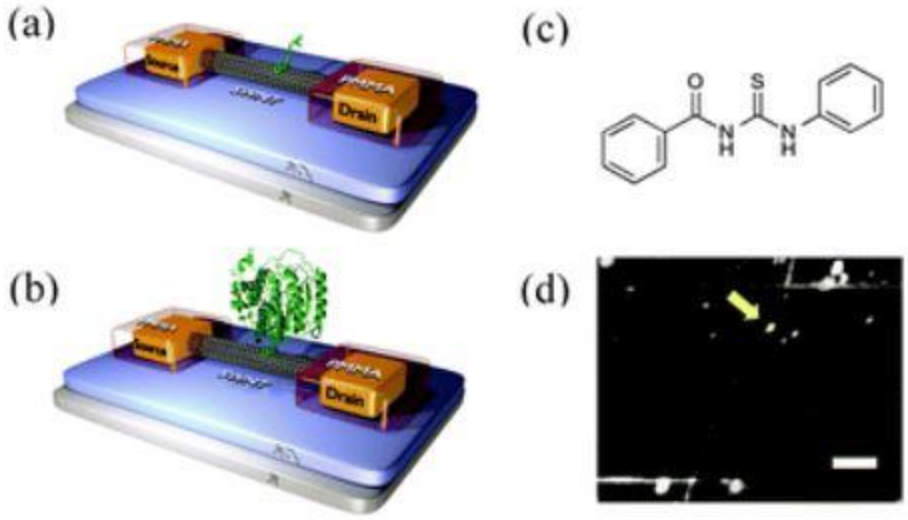

Fig. 5.1: (a) Schematic diagrams of the pSAHA-nanocircuit and (b) the HDAC8-nanocircuit. (c) Chemical structure of the potent activator. (d) An AFM topography image of the single HDAC8 (arrow) attachment on the nanocircuit. The scale bar is 500 nm.

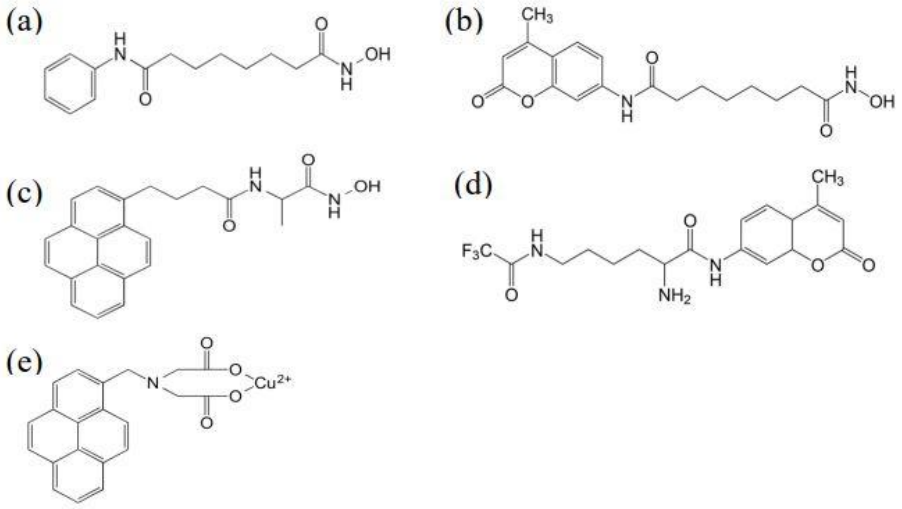

Fig. 5.2: Chemical structures of (a) the SAHA, (b) cSAHA, (c) pSAHA inhibitors, (d) TFALAMC substrate, and (e) a pyrene-IDA-Cu2+ linker.

5.2. Results using the pSAHA-Nanocircuit

5.2.1. Signals from the pSAHA-Nanocircuit

Initially, the conformational dynamics of the HDAC8–pSAHA complex were investigated with the pSAHA-nanocircuit. This configuration allows formation of the complex with the same pSAHA-inhibitor and pre-existing conformational states of individual HDAC8 in bulk solution. 5.3 depicts typical $\Delta I(t)$ signals measured with the pSAHA-nanocircuits. In a buffer solution (25 mM HEPES, 100 mM NaCl, 1 mM TCEP, pH 7.5), the circuit's $\Delta I(t)$ signal shows a featureless baseline current state (Fig. 5.3(a)). Following the addition of HDAC8 (6 μM) to the pSAHA-nanocircuit, an additional current state below the baseline current was observed (Fig. 5.3(b)). $\Delta I(t)$ fluctuated between two current states with a mean amplitude of approximately 4 nA. In addition to HDAC8, the potent activator (ACT, 6 μM) was added to the same circuit (Fig. 5.3(c)). Similar $\Delta I(t)$ fluctuations between two states and the fluctuation rate were observed. Fig. 5.3(d) illustrates a control measurement from the same circuit performed in the presence of both HDAC8 and excess SAHA-inhibitors (30 μM) in the buffer solution. Since the freely-diffusive SAHA-inhibitors surrounding HDAC8 immediately bind to HDAC8 in the solution, no SAHA-free HDAC8 is accessible to the pSAHA-nanocircuit (20), resulting in no $\Delta I(t)$ fluctuations. The absence of the two-level current fluctuation when no HDAC8 is in the solution or when both HDAC8 and excess SAHA-inhibitors are present confirms that $\Delta I(t)$ signals are caused by the HDAC8–pSAHA complex.

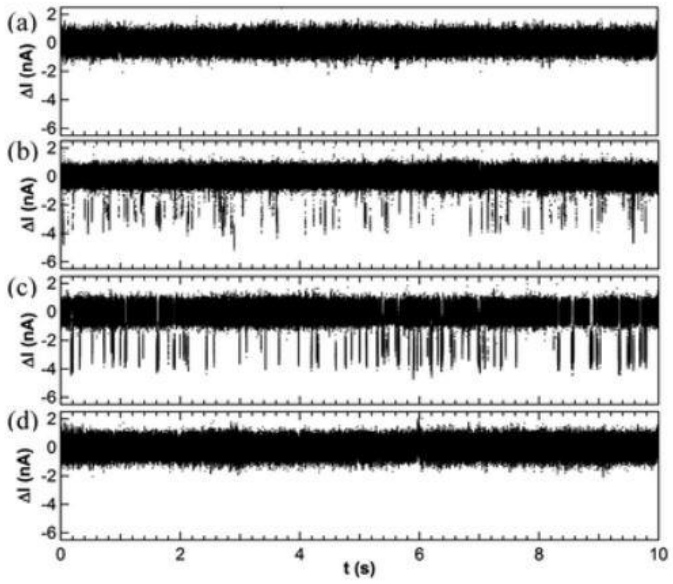

Fig. 5.3: Electronic current Δ*I*(*t*) fluctuations of the pSAHA-nanocircuit. (a) In the absence of HDAC8 (buffer only), no current fluctuations were observed. The addition of (b) the HDAC8 and (c) HDAC8 with the activators resulted in the Δ*I*(*t*) fluctuations between the high-(baseline) and the low-current states corresponding to the conformational transition of the HDAC8–pSAHA complex. (d) A control measurement with excess, freely-diffusive SAHA-inhibitors with HDAC8 in the buffer solution showed no Δ*I*(*t*) fluctuations.

5.2.2. HDAC8 Attachment Mechanism

HDAC8 is known to be a highly flexible enzyme during ligand binding and catalysis (11,21). For SAHA-inhibitors, the hydroxamate acid moiety chelates the metal ions (Zn^{2+}) in the active site pocket, while the aliphatic chain and the capping moiety interact with the hydrophobic pocket and the protein surface (22,23). Crystallographic and computational studies have identified that two loops (L1 and L2) located in the vicinity of the active site pocket entrance are highly malleable to effectively adopt and catalyze structurally different substrates (13,14). While SAHA always remains bound to the metal ions, the two loops dynamically interact to stabilize and catalyze the ligand. When the two loops have open conformations, for example, catalysis takes place. During such conformational rearrangement, motions of charged residues on the loops electrostatically gate the SWNT channel current, resulting in two distinguishable current states. Thus, we assign the low- and high-current states of our signals to the dynamic interaction

of L1 and L2 loops. The low current state and the open loop conformation of the complex could result from negatively charged tri Asp residues (87–89) in the L2 loop moving away from the SWNT (Fig. 5.4) (14).

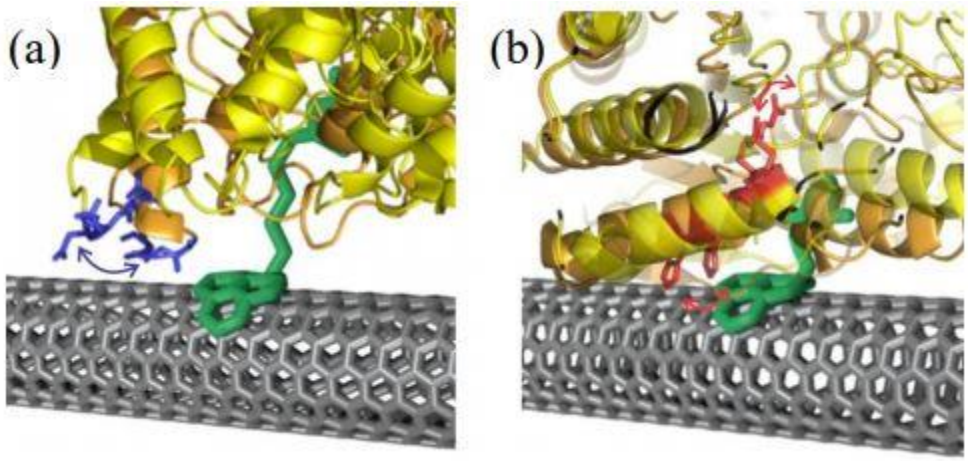

Fig. 5.4: Detailed view of the HDAC8-SWNT interface, showing X-ray structures of the enzyme in its open and closed conformation with (a) pSAHA-nanocircuits and (b) HDAC8-nanocircuits.

5.2.3. HDAC8 Turnover Rates

Fig. 5.5 shows the probability distributions of the duration in the low (τ_{low}) and high (τ_{high}) current states accumulated from 600 s of recordings. All distributions fit simple Poisson distributions, determining single mean values of τ that represent the majority of events (>94%). In the presence of HDAC8 in the buffer solution, the mean values of τ_{low} and τ_{high} were measured to be 1.4 ms and 118 ms, respectively (Fig. 5.5, blue color). In the additional presence of the activators, the mean value of τ_{low} was increased by a factor of 10, but there were no changes in the mean value of τ_{high} (Fig. 5.5, red color). The overall turnover rates, $1/(\tau_{low} + \tau_{high})$, remain almost identical due to the major contribution of τ_{high} to the rates. The long events (<6%) off from the fit at the tail could be intrinsic to HDAC's conformational variability, which affects the arithmetic average $\langle t \rangle$ values of the entire population. The mean values, overall turnover rates, comparable ensemble rates, and relative energy differences are summarized in Table 5.1.

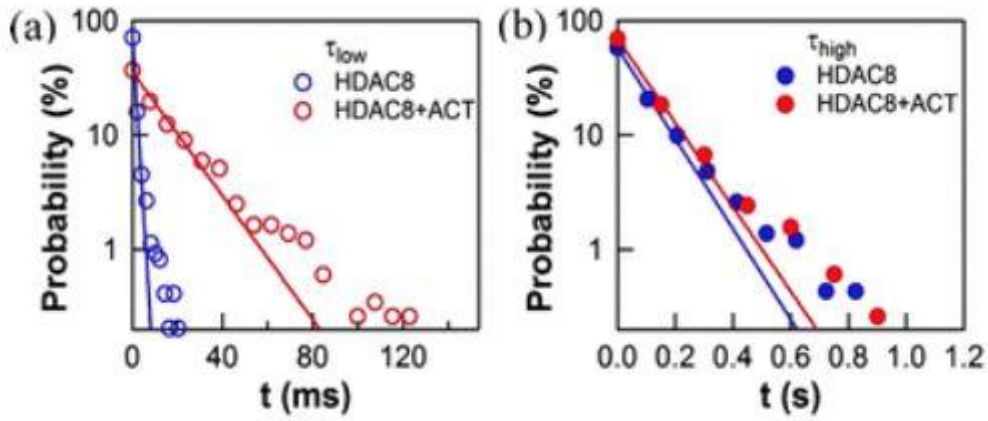

Fig. 5.5: Probability distributions of the duration for two current states: (a) τ_{low} and (b) τ_{high} in the presence and absence of activators. Single exponential fits are shown as solid lines, determining the mean value of τ.

Table 5.1: Kinetic Parameters

	Single-Molecule							Ensemble	
	$\tau_{low}(ms)$	$\langle t_{low}\rangle$(ms)	$\tau_{high}(s)$	$\tau_{high}(s)$	$1/(\tau_{low}+\tau_{high})$ (1/s)	$1/(\tau_{low}+\langle t_{high}\rangle)$ (1/s)	ΔE (kcal/mol)	k_{off}(1/s)	k_{cat}(1/s)
HDAC8	1.40±0.0	2.50±5.60	0.118±0.004	0.170±0.176	8.375	5.799	2.66	21	
HDAC8+ACT	16.4±0.7	22.5±23.5	0.110±0.003	0.152±0.182	7.911	5.731	1.14	0.41-0.77	
cSAHA	13.2±1.2	13.9±12.9	1.360±0.093	2.500±4.030	0.728	0.398	2.78	0.39	
cSAHA+ACT	10.3±0.7	11.3±13.6	1.440±0.010	2.440±3.530	0.690	0.408	2.96	0.39	
TFAL-AMC	54.6±3.7	82.0±96.8	13.35±5.140	13.90±3.570	0.075	0.072	3.30		0.048
TFAL-AMC+ACT	38.5±5.7	63.5±107	12.62±1.771	15.30±19.20	0.079	0.065	3.48		0.048

To complement the single-molecule observation, we performed fluorescence-assay measurements with HDAC8 and pSAHA (Fig. 5.6) The dissociation off-rate (k_{off}) was measured to be 21 s^{-1}. Both a large k_{off} and a relatively short τ_{high} value indicate that pSAHA weakly forms a complex with HDAC8 (22). The orientation and static configuration of the pyrene moiety at the end of a SAHA linker are likely less favorable to contact with the active pocket entrance area of HDAC8. However, the τ_{low} values were significantly increased in the presence of the activator. The activator bound to the inside of the active pocket promotes stabilization of the HDAC8–pSAHA complex, inducing longer loop interaction. Furthermore, the Boltzmann statistics in a

two-state model allow estimating the relative energy ΔE of one state to another state ($\Delta E = k_B T \ln(\langle \tau_{low} \rangle / \langle \tau_{hi} \rangle)$). With the activator, the energy difference is reduced by 43%, resulting in a 12-fold increased τ_{low} (Table 5.1).

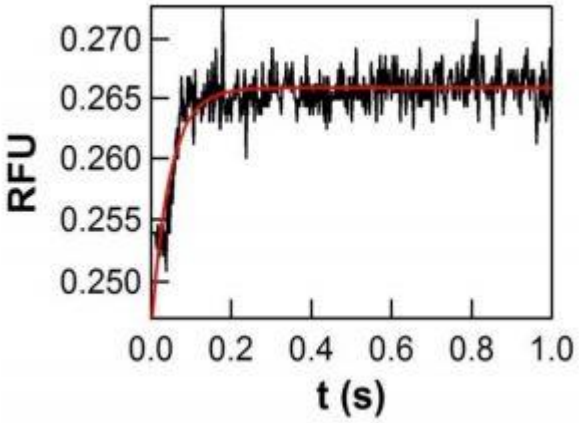

Fig. 5.6: Representative stopped-flow trace for the dissociation of pSAHA from the HDAC8. The red curve is the best fit of the experimental data according to the single exponential rate equation. RFU, relative fluorescence units.

Table 5.2: The Mean Normalized Variance

	r_{low}	r_{high}	r_{high}^{long}
HDAC8	1.21 ± 0.09	1.17 ± 0.08	
HDAC8 + ACT	1.07 ± 0.07	1.30 ± 0.09	
cSAHA	0.86 ± 0.16	1.07 ± 0.19	0.48 ± 0.07
cSAHA + ACT	0.84 ± 0.13	0.93 ± 0.18	0.44 ± 0.06
TFAL-AMC	1.15 ± 0.60	0.64 ± 0.35	
TFAL-AMC + ACT	1.02 ± 0.39	0.70 ± 0.34	

To further examine kinetic information regarding the HDAC8–pSAHA complex, the mean normalized variance $r = \sigma^2 / \langle \tau \rangle^2 = 1/n$ of the τ_{low} and τ_{high} is used to assess the number of hidden intermediate steps (n) during the transition between closed and open loop conformations (Table 5.2) (4,24). The variances, r_{low} and r_{high}, are slightly greater than 1, indicating that the loop opening and closing transition follows a single rate-limiting step process with potential reaction pathways for pre-existing conformational subsets of HDAC8 in bulk solution (24,25).

Thus, the two loops in the complex formation attempt to tighten the weak, non-specific pSAHA inhibitor in the active pocket for the catalytic reaction at the same time.

5.3. Results using the HDAC8-Nanocircuit

5.3.1. Signals from the HDAC8-Nanocircuit

Next, we reversed the configuration of HDAC8 and SAHA (Fig. 5.1(b)) to examine single HDAC8 dynamics with freely-diffusive cSAHA-inhibitors. In the HDAC8-nanocircuit device, the active site pocket of HDAC8 is oriented away from the SWNT, allowing easy access of cSAHA to the pocket entrance areas without a potential interference with SWNTs. The cSAHA has a longer carbon-linker chain than that of pSAHA, which helps cSAHA easily reach to Zn^{2+} ions residing in the deep bottom of the active pocket, and a coumarin moiety at the end of the linker, which gives rise to additional hydrophobic interaction with the active pocket entrance area. In addition, cSAHA has been employed as fluorogenic probes for fluorescence-based binding assays, which permit direct comparisons of the single molecule and ensemble assay results (26).

The electronic recordings show similar $\Delta I(t)$ fluctuating behaviors to the pSAHA-nanocircuit measurements in the presence of cSAHA (5 μM) and cSAHA with the activators (20 μM) (Fig. 5.7(a and b)). For quantitative comparison, probability distributions of the τ_{low} and τ_{high} were generated from 600 s recordings (Fig. 5.7(c and d)). The distributions reasonably fit single exponential distributions, providing mean τ_{low} and τ_{high} values of 13.2 ms and 1.36 s with cSAHA and 10.3 ms and 1.44 s with cSAHA and the activators. However, a substantial population of longer events (16–21%) in the high-current state resulted in bi-exponential distributions with longer time constants (τ^{long}_{high}) of 3.62 s with cSAHA and 4.04 s with cSAHA and the activators.

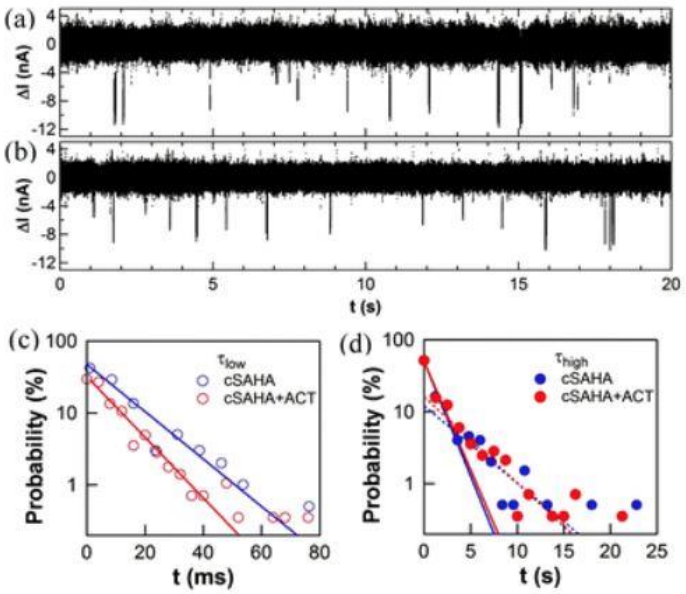

Fig. 5.7: The ΔI(t) fluctuations of the HDAC8-nanocircuit monitored with cSAHA-inhibitors in the (a) absence and (b) presence of the activators. Probability distributions of the (c) τ_{low} and (d) τ_{high} in the presence and absence of activators. The τhigh distribution shows bi-exponential fits (shown as solid and dotted lines)

The τ_{low} value was decreased approximately by 22% with the activator, but the τ_{high} and τ^{long}_{high} were almost identical regardless of the presence of the activators. Accordingly, the relative energy between the two states shows no substantial differences. Instead, the variance analysis resulted in $r_{low} < 1$, indicating two or more rate-limiting steps during the conformational transition of the HDAC8–cSAHA complex. The results suggest that the activator has no significant contribution to the formation of the HDAC8–cSAHA complex. Compared to the pSAHA measurement, τ_{high} values were increased by approximately 10-fold, and accordingly, the overall rates were decreased by 10-fold. As we described above, pSAHA is a weak, non-specific ligand that keeps forming the HDAC8–pSAHA complex, leading to a high frequency of dissociation off-rates and small τ_{low} and τ_{high} values. In contrast, cSAHA has a more favorable structure to form and maintain the HDAC8–cSAHA complex (27). Thus, the longer τ_{high} suggests a longer duration of cSAHA binding to the HDAC8 before the dissociation.

Some of the extra-long duration τ^{long}_{high} could result from the large degree of freedom of cSAHA in the active site pocket to become a stable, catalytically-favorable HDAC–cSAHA complex and a prolonged dissociation process of the cSAHA from the complex.

Our previous fluorescence-assay measurements with cSAHA also show supporting results of the long bound duration and the slow dissociation off-rate, k_{off}, of the HDAC8–cSAHA (Table 5.1) (20). The arithmetic average of overall turnover rates is in strong agreement with ensemble measurements, particularly the observation of the bound duration of the HDAC8–cSAHA complex. The agreement suggests that HDAC8 has two major different pre-existing conformations associated with the τ_{high} and τ^{long}_{high}, which significantly affects the stability of the complex conformation. One of the major conformations could lead to a longer bound duration (τ^{long}_{high}) and its variance value (r^{long}_{high}) of ≈1/2, suggesting two steps with similar rates before or during the loop opening. An additional step during the conformational transitions might be involved in repositioning or reorienting the ligands within the active site for the hydrolysis. Alternatively, the additional step could result from the conformational transition between two microkinetic states of the HDAC8–ligand complex (14).

5.3.2. HDAC8 with TFAL-AMC

Measurements of $\Delta I(t)$ fluctuations with SAHA-inhibitors suggest that dynamic conformational transitions associated with the catalytic activity of the enzymes depend on both the structure of inhibitors and the pre-existing conformation of HDAC8. To further support the catalysis-induced $\Delta I(t)$ fluctuations corresponding to the loop transition of the complex, we monitored $\Delta I(t)$ fluctuations with a HDAC8's cognitive substrate, TFAL-AMC (Fig. 5.8) The $\Delta I(t)$ recordings revealed a few fluctuations for a long duration measurement (>20 min),

indicating a very slow catalytic activity of HDAC8 to the TFAL-AMC substrate. Compared to the SAHA-inhibitors, the loop transition events differ by a factor of 10–100.

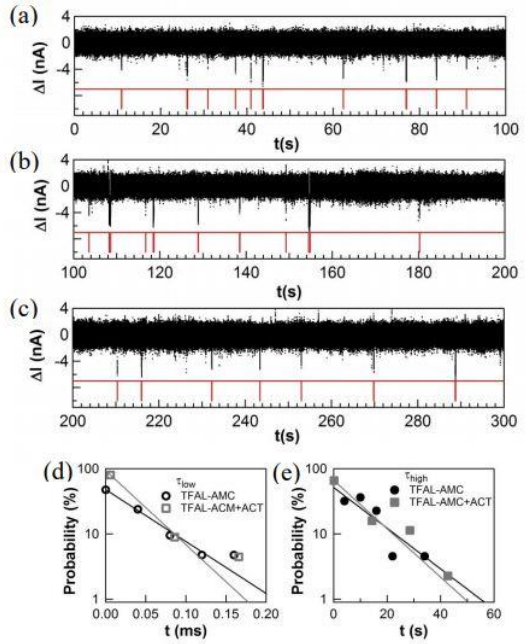

Fig. 5.8: Electronic monitoring of HDAC8's catalytic activities with the TFAL-AMC substrates (a)-(c). Probability distributions of the duration for two current states, (d) τ_{low} and (e) τ_{high}, accumulated from 1200 s of recordings, in the presence and absence of activators. Single exponential fits are shown as solid lines, determining the mean value of τ.

To complement such slow catalytic activity of HDAC8 to the substrate, fluorescent-assay measurements were performed. Using standard Michaelis–Menten methods, the catalytic turnover rate was measured to be 0.048 s^{-1} (Fig. 5.9) This rate is in agreement with the conformational transition rate (0.072–0.065 s^{-1}) from the single molecule electronic measurements. Thus, we further conclude that the two-level $\Delta I(t)$ fluctuation is caused by the catalysis-induced conformational transition of loops in the complex.

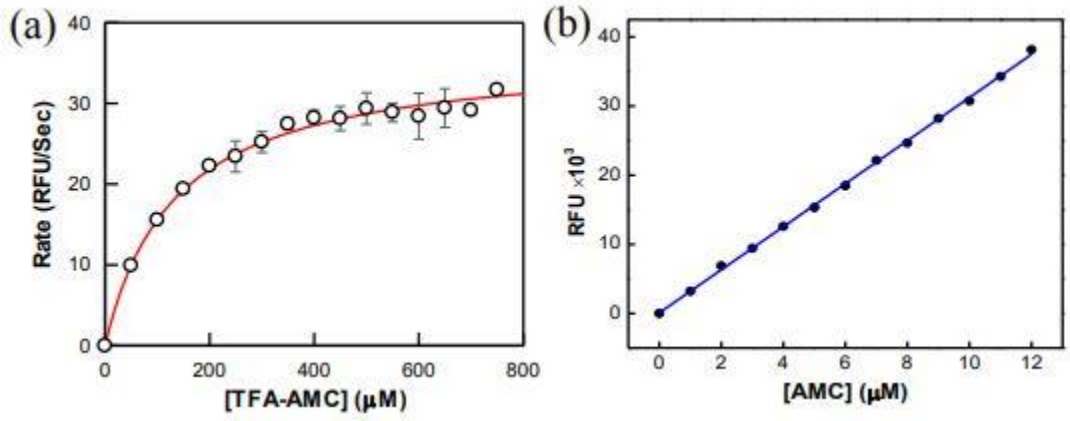

Fig. 5.9: (a) The initial rate of the HDAC8 catalyzed reaction as a function of substrate (TFAL-AMC) concentration. The solid line is the best fit of the data using the Michealis-Menten equation with Km and Vmax values of 134 ± 3 μM and 36 ± 1 RFU/sec. The Vmax value thus derived was converted to kcat (0.049 s-1) using the standard curve of the fluorescence emission intensity vs. fluorophore (AMC) concentration. No effect of the activator in the same measurements was observed.

Although both single molecule and ensemble-assay measurements show no significant enhancement of the catalytic turnover rates by the activators, the τ_{low} value was modestly decreased (Table 5.1). The decreased time spent in the catalysis-ready, open loop conformation resulted in an approximately 29% decrease in the catalytic reaction time. Moreover, the variance of $r_{low} \approx 1$ indicates a simple, transient deacetylation by HDAC8. However, the variance of $r_{hi} \approx$ 0.64–0.70 suggests that multiple steps are involved in the HDAC8–TFAL-AMC complex including conformational transition and dissociation of product steps (13). Taken together, the activators minimally and selectively contribute to the HDAC8–TFAL-AMC complex and catalysis.

5.4. Nanocircuit Monitoring of Single HDAC8 Dynamics Summary

In conclusion, the electronic readouts directly visualized real-time trajectories of HDAC8–ligand interaction and revealed the number of key rate-limiting steps during the ligand binding and catalysis. Specifically, the following observations provide new insights into the kinetics of the HDAC8–ligand interaction: (1) a substantial conformational rearrangement

between two ordered conformational states occurs in the binary complex; (2) the small molecule activator enhances the binding affinity of the weak inhibitor/ligand to the active site pocket of the enzyme and stabilizes the binary complex; (3) a single rate-liming step occurs during the closed loop conformation; and (4) two or more steps for either the ligands' reorientation or the product release take place during or after open loop conformation.

5.5. References

1. Z. D. Nagel and J. P. Klinman, Nat. Chem. Biol., 2009, 5, 543–550.
2. L. Meireles, M. Gur, A. Bakan and I. Bahar, Protein Sci., 2011, 20, 1645–1658.
3. G. Bhabha, J. Lee, D. C. Ekiert, J. Gam, I. A. Wilson, H. J. Dyson, S. J. Benkovic and P. E. Wright, Science, 2011, 332, 234–238.
4. W. Min, B. P. English, G. Luo, B. J. Cherayil, S. C. Kou and X. S. Xie, Acc. Chem. Res., 2005, 38, 923–931.
5. J. A. Erickson, M. Jalaie, D. H. Robertson, R. A. Lewis and M. Vieth, J. Med. Chem., 2004, 47, 45–55.
6. Y. He, M. Lu, J. Cao and H. P. Lu, ACS Nano, 2012, 6, 1221–1229.
7. J. Graff and L. H. Tsai, Nat. Rev. Neurosci., 2013, 14, 97–111.
8. N. A. Wolfson, C. A. Pitcairn and C. A. Fierke, Biopolymers, 2013, 99, 112–126.
9. L. Verdone, M. Caserta and E. Di Mauro, Biochem. Cell Biol., 2005, 83, 344–353.
10. P. M. Lombardi, K. E. Cole, D. P. Dowling and D. W. Christianson, Curr. Opin. Struct. Biol., 2011, 21, 735–743.
11. N. Deschamps, C. A. Simoes-Pires, P. A. Carrupt and A. Nurisso, Drug Discovery Today, 2015, 20, 736–742.

12. J. R. Somoza, R. J. Skene, B. A. Katz, C. Mol, J. D. Ho, A. J. Jennings, C. Luong, A. Arvai, J. J. Buggy, E. Chi, J. Tang, B. C. Sang, E. Verner, R. Wynands, E. M. Leahy, D. R. Dougan, G. Snell, M. Navre, M. W. Knuth, R. V. Swanson, D. E. McRee and L. W. Tari, Structure, 2004, 12, 1325–1334.

13. G. Estiu, N. West, R. Mazitschek, E. Greenberg, J. E. Bradner and O. Wiest, Bioorg. Med. Chem., 2010, 18, 4103–4110.

14. M. B. Kunze, D. W. Wright, N. D. Werbeck, J. Kirkpatrick, P. V. Coveney and D. F. Hansen, J. Am. Chem. Soc., 2013, 135, 17862–17868.

15. Y. Choi, I. S. Moody, P. C. Sims, S. R. Hunt, B. L. Corso, D. E. Seitz, L. C. Blaszcazk, P. G. Collins and G. A. Weiss, J. Am. Chem. Soc., 2012, 134, 2032.

16. M. V. Akhterov, Y. Choi, T. J. Olsen, P. C. Sims, M. Iftikhar, O. T. Gul, B. L. Corso, G. A. Weiss and P. G. Collins, ACS Chem. Biol., 2015, 10, 1495–1501.

17. Y. Choi, I. S. Moody, P. C. Sims, S. R. Hunt, B. L. Corso, G. A. Weiss and P. G. Collins, Science, 2012, 335, 319–324.

18. Y. Choi, T. J. Olsen, P. C. Sims, I. S. Moody, B. L. Corso, M. N. Dang, G. A. Weiss and P. G. Collins, Nano Lett., 2013, 13, 625–631.

19. R. K. Singh, T. Mandal, N. Balsubramanian, T. Viaene, T. Leedahl, N. Sule, G. Cook and D. K. Srivastava, Bioorg. Med. Chem. Lett., 2011, 21, 5920–5923.

20. R. K. Singh, K. Cho, S. K. Padi, J. Yu, M. Haldar, T. Mandal, C. Yan, G. Cook, B. Guo, S. Mallik and D. K. Srivastava, J. Biol. Chem., 2015, 290, 6607–6619.

21. C. Decroos, D. J. Clausen, B. E. Haines, O. Wiest, R. M. Williams and D. W. Christianson, Biochemistry, 2015, 54, 2126–2135.

22. M. S. Finnin, J. R. Donigian, A. Cohen, V. M. Richon, R. A. Rifkind, P. A. Marks, R. Breslow and N. P. Pavletich, Nature, 1999, 401, 188–193.

23. A. Vannini, C. Volpari, G. Filocamo, E. C. Casavola, M. Brunetti, D. Renzoni, P. Chakravarty, C. Paolini, R. De Francesco, P. Gallinari, C. Steinkuhler and S. Di Marco, Proc. Natl. Acad. Sci. U. S. A., 2004, 101, 15064–15069.

24. W. Xu, J. S. Kong and P. Chen, J. Phys. Chem. C, 2009, 113, 2393–2404.

25. D. Zheng and H. P. Lu, J. Phys. Chem. B, 2014, 118, 9128–9140.

26. R. K. Singh, T. Mandal, N. Balasubramanian, G. Cook and D. K. Srivastava, Anal. Biochem., 2011, 408, 309–315.

27. D. P. Dowling, S. L. Gantt, S. G. Gattis, C. A. Fierke and D. W. Christianson, Biochemistry, 2008, 47, 13554–13563.

CHAPTER 6. DETECTION OF PANCREATIC CANCER EXOSOMES WITH GRAPHENE FIELD EFFECT TRANSISTORS

6.1. Pancreatic Cancer Detection Introduction

6.1.1. Importance of Studying Pancreatic Cancer Detection

More than 45,000 people die from pancreatic cancer per year in the United States alone (1), and the five year survival rate of pancreatic ductal adenocarcinoma (the most common type of pancreatic cancer, abbreviated PDAC) is less than five percent (2). This high mortality rate stems from pancreatic cancer not having noticeable external symptoms in the early stages of development, resulting in late stage diagnosis (2). Thus, early detection is critical to the cancer treatment process, similar to how pap smears, mammograms and colonoscopies have dramatically reduced the death rates for cervical (3), breast (4), and colon cancers (5) respectively. Unfortunately, existing detection methods for pancreatic cancer, such as biopsies, are invasive, difficult and are prone to giving false-negatives (6, 7).

A reliable screening method for pancreatic cancer, capable of detection in the early stages, would therefore greatly increase patients' survival rates. What we are presenting here is a novel electronic method of pancreatic cancer detection capable of sensing exosomes (8-10), a type of vesicle that is released by pancreatic tumor cells (6), in real-time with concentrations consistent to that which can be found in the blood of a human with pancreatic cancer.

In addition, by varying the linker peptide, our method could potentially be expanded to detect exosomes from other types of diseases and cancers as well, leading to an entirely new method of diagnosis (11).

6.1.2. Graphene Transistors as Screening Devices

Recently, graphene transistors have gained much attention due to their high sensitivity to surface activity, rising from the low dimensionality of graphene (12,13). Additionally, functionalization of the graphene's surface with linker molecules gives the nano-devices selectivity that can be utilized in the real-time detection of various biological targets and gases such as DNA and nitric oxide (11,12). Sub-nanomolar sensitivity and the ability to functionalize the graphene to selectively bind to detection targets make these nano-devices a natural choice for the real-time detection of pancreatic cancer exosomes (14).

6.1.3. Exosomes as Biomarkers

The tripeptide (Arg-Gly-Asp, RGD) is the most common peptide motif facilitating adhesion between the extracellular matrix (ECM) and cells. It functions by being recognizable to integrins (adhesion proteins) that bind to them. Pancreatic tumor cells have been shown to overexpress the integrins $\alpha_v\beta_3$ and $\alpha_v\beta_5$ compared to healthy cells. Also, the cyclic peptide, iRGD (CRGDK/RGPD/EC), has been proven to strongly bind to these overexpressed integrins on the tumor cell surfaces, allowing this peptide to target tumors for drug delivery (15,16).

Meanwhile, exosomes are vesicles formed in the endosomal compartment of the majority of eukaryotic cells by means of multi-vesicular bodies (MVBs) fusing with the cell surface instead of lysosomes, causing the vesicle to detach from the cell into the surrounding medium (8-10). Present in every biological fluid, and containing information from the parent cell, such as the DNA, RNA, and lipids, exosomes would make ideal biomarkers for a plethora of different medical conditions. In particular, exosomes from pancreatic cancer tumors can be found in the bloodstream and their membranes contain the same overexpression of the integrins $\alpha_v\beta_3$ and $\alpha_v\beta_5$, as the pancreatic cancer cells they originate from (17). This allows them to be

distinguished from other exosomes and bioparticles in the bloodstream and makes these integrins ideal targets for the selective detection of pancreatic cancer exosomes.

Therefore, by modifying the iRGD peptide with a pyrene end (creating pyrene-iRGD) and decorating the graphene surface with the pyrene-iRGD peptide, we can create nanoscale sensors that selectively detect pancreatic cancer exosomes. Exosomes bound to the graphene surface and their surface charges electrostatically gate the graphene transistor and trigger a response in the electric current.

6.2. Fabrication of Graphene Device and Functionalization with iRGD

6.2.1. Graphene Device Fabrication

Graphene biosensor chips are fabricated on standard 4" silicon wafer using conventional processing techniques (18), The process starts with silicon wafer with patterned Ti/Pt electrodes, including the source, drain, counter and reference electrodes, using a liftoff process. Wafers are then cleaned by piranha etching to remove all potential organic residues from the liftoff process, which will potentially degrade the performance of graphene biosensors. Concurrently with the electrodes patterning, high quality graphene films are grown in tube furnaces at temperatures exceeding 1030◦C on copper foil using standard chemical vapor deposition method as reported in the literature (19). Graphene films are spin coated with a PMMA support layer, then delaminated from the copper foil growth substrate by bubbling transfer as described in the literature (20). The graphene films are deposited on top of the electrode-patterned wafers and thoroughly cleaned with acetone and isopropanol to remove the PMMA support layer, and then annealed with forming gas at 200C for 1 hour. The final fabrication stage consists of patterning the graphene sheets into defined channels between the source-drain electrodes and then passivating the Ti/Pt

electrodes with a plasma-enhanced CVD silicon oxide layer on the entire wafer. Finally, the graphene strips are released using reactive ion etching.

After the fabrication process, all graphene biosensors must go through a thorough quality assurance process, including optical and electrical quality assurance to rule out any underperformed biosensors. The accepted biosensors have clean graphene surface with electrical resistance of 2 ~ 50kΩ. The average Dirac point in this collection of devices is 21.78V ± 2.67V and the average hole mobility is 4945 cm^2/Vs ± 2000 cm^2/Vs in ambient, and the average two terminal resistance is 6085 (unit)± 1838 (unit), indicating very high quality graphene with high consistency.

6.2.2. Integration with Microfluidic Channel

The whole circuit is then placed inside a 2 µl microfluidic chamber with an incoming channel and an outgoing channel. A schematic of this setup can be viewed in Figure 6.1. Exosomes passing through the channel will enter the chamber and be exposed to the RGD-functionalized graphene surface. Exosomes over-expressing $\alpha_v\beta_3$, and $\alpha_v\beta_5$ (pancreatic cancer exosomes) will then attach to the graphene surface while normal cells do not interact. As the cancer exosomes bind to the surface, surface charges of the exosomes interact with the graphene and effectively gate the transistor, allowing for real-time, selective detection of pancreatic cancer cells.

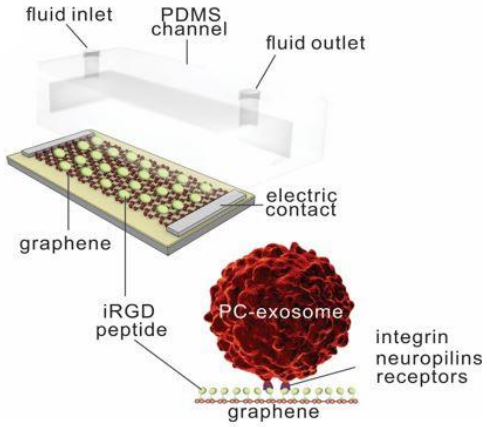

Fig. 6.1: Schematic of graphene field effect transistor including attached pyrene-iRGD and microfluidic channel. Also included is a depiction of a pancreatic cancer exosome binding to the iRGD coated graphene surface.

6.2.3. Functionalization with Pyrene-iRGD

We were successfully able to functionalize graphene with RGD peptides by attaching a pyrene foot to the RGD (pyrene-iRGD) that bonded through non-damaging, non-covalent pi-pi stacking to the graphene surface. Attachment of pyrene-iRGD was confirmed through multiple methods.

First, by measuring the height of the graphene strip with an AFM before and after functionalization, it was observed that there was a 0.5 nm height increase of the graphene strip after pyrene-iRGD attachment shown in Figures 6.2.

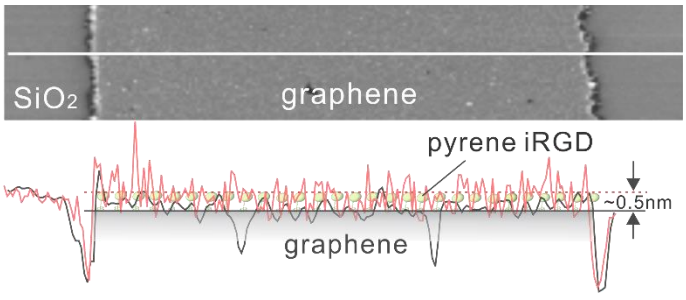

Fig. 6.2: AFM image of graphene surface with pyrene-iRGD and height profile of the same location before and after pyrene-iRGD functionalization. There is a 0.5 nm height increase after the addition of the linker molecule and the surface becomes much rougher due to being covered in peptides.

6.2.4. Detection of Pancreatic Cancer Exosomes from PANC-1 Cell Line

As an initial test of the device's ability to detect exosomes, we performed a simple experiment where we coated the graphene surface with pyrene-iRGD, and then after placing the device inside the microfluidic channel, we injected exosome-less phosphate buffer solution (PBS) into the channel while measuring the source-drain current. Then a PBS solution containing healthy exosomes was injected into the channel, however, since these healthy exosomes do not overexpress the α_v integrins, nothing attached to the graphene surface, the current remained flat.

This same experiment was then repeated, but instead of injecting healthy exosomes into the channel, increasing concentrations of pancreatic cancer exosomes from the PANC-1 cell line were injected, starting at low to high concentration being injected. As the number of pancreatic cancer exosomes exposed to the graphene increased, the current decreased, eventually causing a total current drop of about 200 nA. These current drops are due to the pancreatic cancer exosomes binding to the iRGD on the graphene and gating the device.

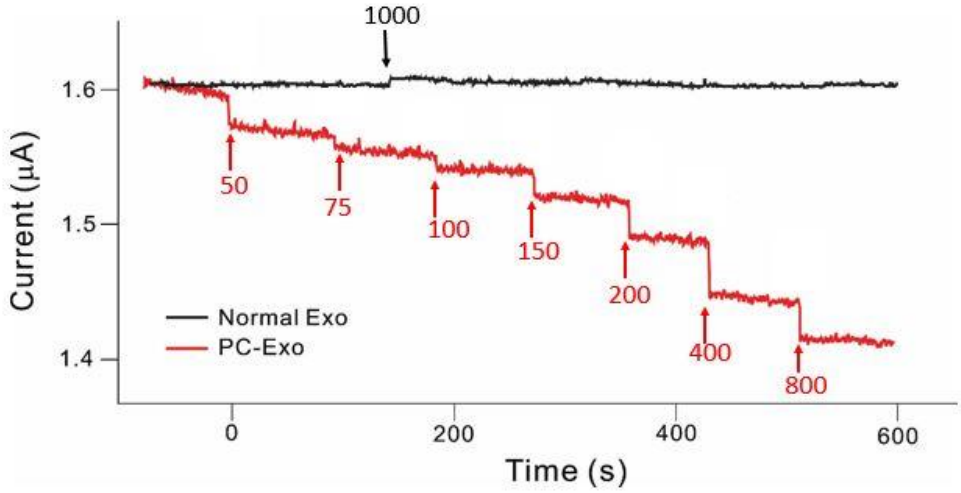

Fig. 6.3: Real-time current measurement while exposing the graphene phosphate buffer solution (PBS) and then increasing numbers of exosomes. The black line represents the current while exposing the graphene to normal healthy exosomes. Before the 1000 mark, the graphene is only exposed to PBS, afterwards 1000 normal exosomes were injected into the channel. The red line represents the current while exposing the graphene to PBS, and then increasing the numbers of pancreatic cancer exosomes in the channel. The numbers represent the number of new exosomes added at that point. The number of exosomes in the microfluidic cells are roughly estimated by protein concentration.

The iRGD binding with $\alpha_v\beta_3$, and $\alpha_v\beta_5$ depends on the presence of divalent cations (charge of +2) at the binding site (21,22). Since this is the region that likely binds the strongest to the iRGD attached to the graphene surface, it is also the region that likely exerts the most direct electric field onto the surface, thus positively gating the graphene surface and causing a decrease in the graphene's conductivity and the current through the transistor. This explains why the measured current decreases in Figure 6.3.

6.2.5. Confirming the Role of iRGD in Exosome Attachment

Additional control AFM experiments were performed to confirm that the iRGD is responsible for exosome attachment to the graphene. In these tests, instead of putting the graphene device in the microfluidic channel and connecting the electrodes to the probestation to measure its current, the device was placed in a closed plastic dish to prevent evaporation, and

then a droplet from each sample was incubated on top of the chip for twenty minutes, followed by a rinse with buffer and tween, and then dried by N^2 gas. Afterwards, the graphene surface was imaged with an AFM to see what differences there were to the surface.

The first sample to be incubated on the graphene surface was a PBS sample containing exosomes from healthy human cells. This sample was incubated on the graphene surface after the surface had been decorated with pyrene-iRGD. Afterwards, once the device had been imaged with the AFM, there was no observable difference between the post-incubation graphene surface and the pre-incubation graphene surface. This is due to the control exosomes not being able to attach to the pyrene-iRGD on the graphene surface. Some non-specific binding likely occurred, but exosomes attached that way would have been washed off by the tween. Both the before and after images of the graphene surface can be seen in Figure 6.4(a) and (b).

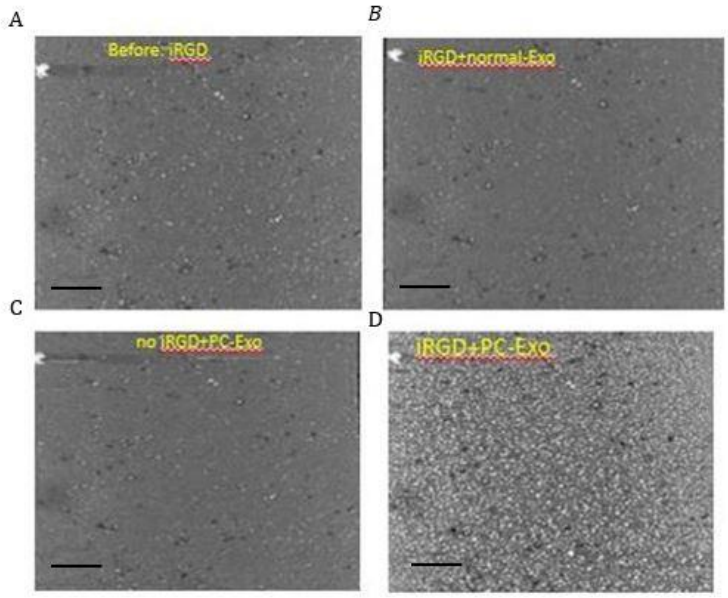

Fig. 6.4: AFM images of (a) graphene surface pre-incubation, (b) incubated with attached pyrene-iRGD and healthy exosomes, (c) with no pyrene-iRGD and pancreatic cancer exosomes, and (d) with pyrene-iRGD and pancreatic cancer exosomes. All scale bars are 1μm.

Next, a PBS sample containing exosomes from pancreatic cancer cells were incubated on a graphene device that had not been covered in pyrene-iRGD. Since there were no peptides for

the exosomes to attach to, the AFM image taken afterwards revealed no exosomes attached to the graphene surface, as can be seen in Figure 6.4(c).

Finally, a similar sample containing pancreatic cancer exosomes was incubated on a graphene device that had been coated in pyrene-iRGD. This time, when the device was imaged with the AFM afterwards, it was clearly covered in many exosomes that had attached to the surface (Figure 6.4 (d)). This series of experiments were duplicates of the experiments that resulted in the images in Figure 6.3. Likewise, they proved the ability of our detection method to selectively detect exosomes that originated from pancreatic cancer tumors and that the pyrene-iRGD covering the graphene surface is the key mechanism controlling exosome attachment to the graphene surface.

6.2.6. Western Blot Analysis of Exosome Types

After confirming that the pancreatic cancer exosomes will selectively bind to the iRGD, we wanted to examine the differences in exosomes that came from different pancreatic cancer cell lines and analyze the expression levels of the target integrins in the different exosomes. In order to accomplish this, we performed western blot analyses on the different exosome samples, including pancreatic cancer exosomes from the PANC-1 cell line as well as normal and HPNE exosomes. After performing these tests, it was clear that the exosomes from the cancer cell lines expressed the α_v and β_5 integrins at a much higher level than the noncancerous exosomes (Figure 6.5). This obvious overexpression of the target integrins strengthens our position that these integrins are indeed what the iRGD is binding to.

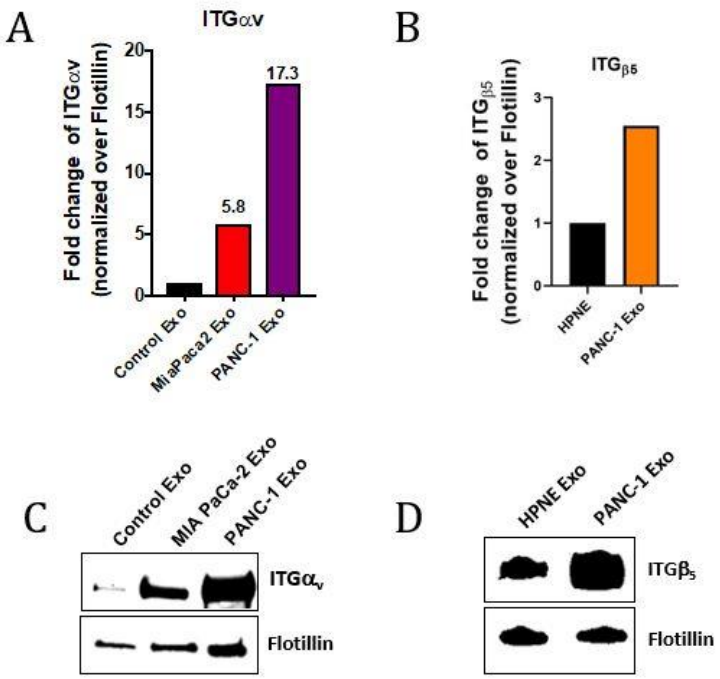

Fig. 6.5: (a,b) Bar graphs of western blot expression levels of α_v and β_5 integrins for pancreatic cancer exosomes from the PANC1 and MIA-PaCa 2 cell line as well as healthy exosomes (HPNE). (c,d) Western blot analyses of those same exosome types.

6.2.7. Blocking Integrins with Free-iRGD

At this point, we had shown that the interaction with the attached pyrene-iRGD was what allowed the pancreatic cancer exosomes to bind to the graphene surface and that the pancreatic cancer exosomes overexpressed $\alpha_v\beta_3$ and $\alpha_v\beta_5$ which were the target receptors for the iRGD. We had also shown that our graphene device coated with pyrene-iRGD specifically detected pancreatic cancer exosomes over healthy control exosomes, which strongly implies that the iRGD interactions with the overexpressed integrins were what controlled the binding mechanism between the graphene surface and the pancreatic cancer exosomes, but we wanted to confirm this further, so we designed another control experiment to prove that the integrin were responsible for the pancreatic cancer exosomes binding to the device's surface.

This experiment consisted of using the previously described setup of placing the pyrene-iRGD coated graphene device inside of the microfluidic channel, and then measuring the electric current while injecting samples of increasing exosome concentration into the channel. For this control measurement, we started by injecting a sample of only PBS into the channel and then two samples with increasing concentrations of exosomes from the PANC-1 cell line. As before, as the concentration increased, the electric current decreased.

We then repeated this same procedure, but after mixing 5 mg/ml of free iRGD peptides into the samples containing pancreatic cancer exosomes. When these samples were injected into the microfluidic channel, they induced a drop in the electric current, however, the decrease in current was approximately a third of current drop caused by the pancreatic cancer exosomes without the free iRGD. This implies that fewer exosomes were attaching to the graphene surface, and the reason for that was that the free iRGD were also binding with the overexpressed integrins of the pancreatic cancer exosomes. As the free iRGD bound to the integrins, they occupied the active site of the $\alpha_v\beta_3$ and $\alpha_v\beta_5$ and blocked them from being able to attach to the pyrene-iRGD covering the graphene surface, thus resulting in fewer exosome attachments and a smaller drop in the electric current (Figure 6.6).

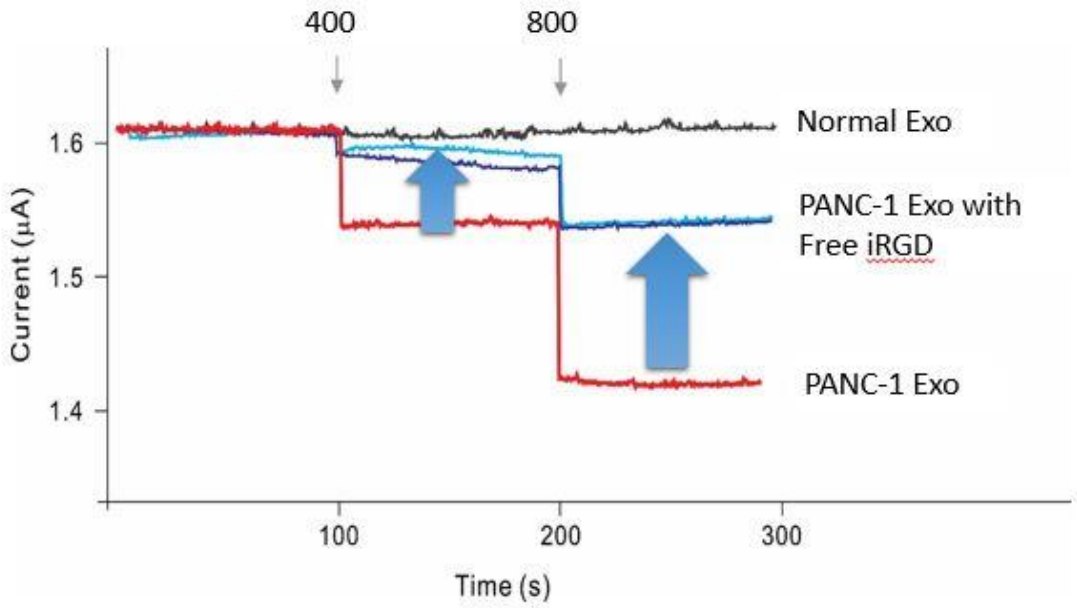

Fig. 6.6: Real-time current measurements while exposing the graphene to high concentrations of normal exosomes, PANC-1 exosomes, and PANC-1 exosomes pre-incubated with 5 mg/ml of free iRGD. It is clear that after incubating with free iRGD that the PANC-1 exosomes did not cause as large of current changes. This is due to the free iRGD blocking some of the α_v integrins and preventing as much attachment.

6.3. Real Patient Samples

6.3.1 Patient Sample Introduction

All of the detection experiments before now had been with exosomes gathered from pancreatic cancer cell lines grown in the lab of our collaborator, so the next step in proving our method's ability to diagnose patients with pancreatic cancer was to use our method to detect pancreatic cancer exosomes from actual hospital patients. For this part of the project, we collaborated with Dr. Randall Brand (University of Pittsburgh Medical Center) to obtain blood samples from patients with and without pancreatic cancer and with different stages of pancreatic cancer. Additionally, up to this point, the pancreatic cancer cell lines we have been using were from the most common and aggressive form of pancreatic cancer called pancreatic adenocarcinoma (PDAC) which is responsible for approximately 85% of pancreatic cancer cases.

Therefore, the majority of patient samples we tested with pancreatic cancer were from patients with PDAC.

6.3.2. Initial Patient Sample Tests

The first experiment we performed consisted of two known patient samples, one with stage four pancreatic cancer, and one with a healthy control pancreas. The exosomes were separated from the blood and human serum using the centrifuge method described earlier, and then the graphene was decorated with pyrene-iRGD and placed inside the microfluidic channel. Then, a sample of only PBS was injected into the microfluidic channel to get a baseline current. After that, the sample containing stage four pancreatic cancer exosomes was injected into the channel, and a large current drop of over 200 nA was observed (Figure 6.7 (a) and (b)).

This experiment was repeated, but with the sample from the patient with a normal pancreas. When this sample was injected into the channel, it caused an electric current drop of approximately 30 nA, which was easily distinguishable from the larger current drop induced by the stage four pancreatic cancer sample. To further confirm that these current changes were being caused by exosomes in the two patient samples, we diluted both samples to a third of their original concentration. After dilution, we repeated the previous two measurements, but with the diluted samples, and observed that for both patient samples, the diluted samples caused smaller current changes than the samples with higher exosome concentrations. This confirmed that exosomes in the patient samples were responsible for the measured current changes.

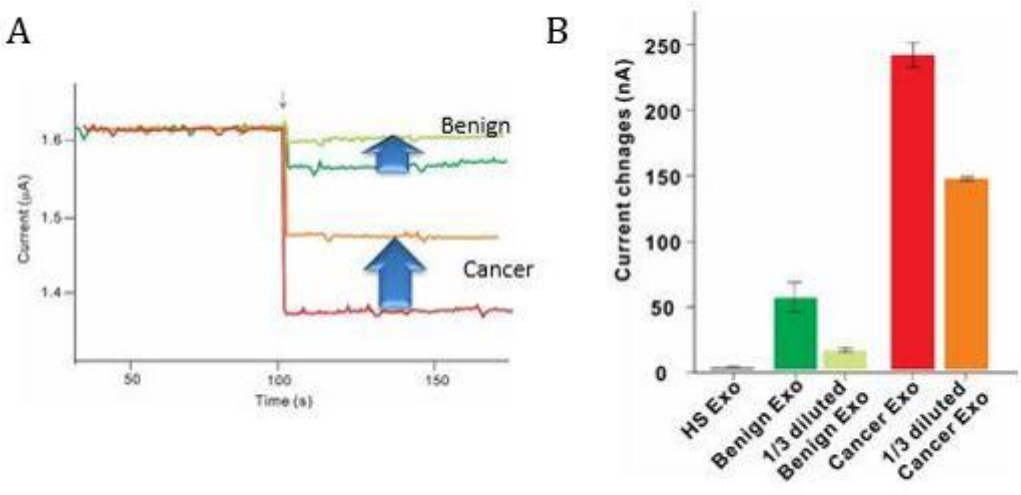

Fig. 6.7: (a) Real-time current measurements while exposing the graphene to exosome samples from a healthy patient, and a patient with stage 4 pancreatic cancer at full and one-third concentrations. (b) Bar graph analyzing current changes from (a).

6.3.3. Additional Patient Sample Tests

Encouraged by these results, we continued testing more patient samples including more samples from patients with healthy pancreases and from patients with pancreatic cancer. In addition, we tested samples from patients with chronic pancreatitis, which is a condition other screening methods often confuse with pancreatic cancer (23). We repeated the measurement three times with each sample and included the average of the three with error bars in the bar graph of Figure 6.8. From this graph, it is easily apparent that our method current changes caused by the pancreatic cancer exosomes are distinguishable from the current changes induced by the other types of patient samples including the chronic pancreatitis samples. The noncancerous samples corresponded to current changes of below 100 nA, and the pancreatic cancer samples induced changes between approximately 200 and 400 nA. This large difference in current changes is a strong indicator that our method is successfully able to screen for pancreatic cancer.

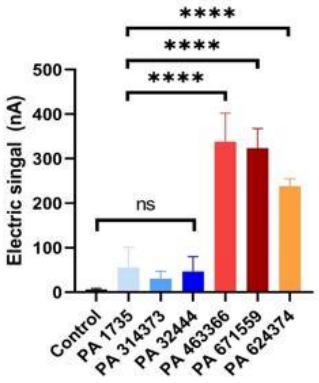

Patient Number	Condition
1735	Chronic Pancreatitis
314373	Normal Pancreas
32444	Normal Pancreas
463366	PDAC
671559	PDAC
624374	PDAC

Fig. 6.8: (a) Bar graph of measured current change induced by graphene exposure to a normal cell line sample, and samples from patients with conditions including chronic pancreatitis, normal pancreas and pancreatic ductal adenocarcinoma (PDAC, the most common type of pancreatic cancer). Three measurements were taken using each sample to establish the error. This clearly illustrates the ability of our method to distinguish between pancreatic cancer and noncancerous samples with a p-value of less than 0.00001. Also included is a chart of which condition corresponds with which patient.

6.4. Summary of Pancreatic Cancer Exosome Detection

Early detection is critical for the successful treatment of pancreatic cancer (2). Unfortunately, due to a lack of progress in this area, the likelihood of surviving a pancreatic cancer diagnosis is dismal due to the cancer having already advanced to metastasis by the time it is discovered, due to the invasiveness, difficulty, and unreliability of diagnosis techniques (6,7). Thus, it is critical to develop an easy low-cost method of testing for pancreatic cancer.

The research we present here consists of fabricating a graphene field-effect transistor and functionalizing the graphene surface with pyrene-iRGD, a peptide that specifically binds to receptors on the surface of pancreatic cancer biomarkers known as exosomes. Our studies revealed that our method was capable of sensitively and specifically detecting pancreatic cancer

exosomes and that while measuring the electric current through the device, if the device was exposed to these biomarkers, there would be a measurable decrease in the electric current, allowing for the identification of pancreatic cancer exosomes.

We also performed tests on real patient samples of samples from a patient with a benign tumor and a patient with a pancreatic cancer tumor. Our test was successfully, and easily able to distinguish the two which is a very promising result.

Future work in this area would involve performing more blind tests to build up statistics on the accuracy of our test, and to test more samples from patients in the early stages of the cancer to find how effective our method would be at early stage diagnosis.

6.5. References

1. R. L. Siegel, K. D Miller, A. Jemal, CA Cacer J Clin, 2019, 69, 7-34.
2. S. R. Hingorani, E. F. Petricoin III, A. Maitra, V. Rajapakse, C. King, M. A. Jacobetz, S. Ross, T. P. Conrads, T. D. Veenstra, B. A. Hitt, Y. Kawaguchi, D. Johann, L. A. Liotta, H. C. Crawford, M. E. Putt, T. Jacks, C. V. E. Wright, R. H. Hruban, A. M. Lowry, D. A. Tuveson, Cancer Cell, 2003.
3. J. Peto, C. Gilham, O. Fletcher, F. E. Matthews, The Lancet, 2004, 9430, 249-256.
4. R. E. Hendrick, M. A. Helvie, American Journal of Roentgenology, 2011, 2.
5. J. M. Inadomi, A. Sonnenberg, Gastrointestinal Endoscopy, 2000, 51, 517-523.
6. S. S. Kanwar, C. J. Dunlay, D. M. Simeone, S. Nagrath, Lab on a Chip, 2014, 14, 1891.
7. F. Gress, K. Gottlieb, S. Sherman, G. Lehman, Annals of Internal Medicine, 2001.
8. C. Thery, K. W. Witwer, et. al., Journal of Extracellular Vesicles, 2018, 7.
9. M. Yanez-Mo, P. R.-M. Siljander, Z. Andreu, et. al., Journal of Extracellular Vesicles, 2015, 1.

10. G. van Niel, G. D'Angelo, G. Raposo, Nature Reviews Molecular Cell Biology, 2018, 19, 213-228.

11. A. V. Vlassoz, S. Magdaleno, R. Setterquist, R. Conrad, Biochimica et Biophysica Acta (BBA)-General Subjects, 2012, 1820, 940-948.

12. A. K. Manoharan, S. Chinnathambi, R. Jayavel, N. Hanagata, Science and Technology of Advanced Materials, 2016, 18, 43-50.

13. S. Jiang, R. Cheng, X. Wang, T. Xue, Y. Liu, A. Nel, Y. Huang, X. Duan, Nature Communications, 2013.

14. S. A. Melo, L. B. Luecke, C. Kalhert, et. al., Nature, 2015, 523, 177-182.

15. K. N. Sugahara, T. Teesalu, P. P. Karmali, V. R. Kotamraju, L. Agemy, O. M. Girard, D. Hanahan, R. F. Mattrey, E. Ruostahti, Cancer Cell, 2009.

16. T. Teesalu, K. N. Sugahara, V. R. Kotamraju, E. Ruostahti, Proceedings of the National Academy of Sciences, 2009.

17. E. van der Pol, A. Boing, P. Harrison, A. Sturk, R. Nieuwland, Pharmacological Reviews, 2012, 64, 676-705.

18. M. B. Lerner, D. Pan, Y. Gao, L. E. Locascio, K.-Y. Lee, J. Nokes, S. Afsahi, J. D. Lerner, A. Walker, P. G. Collins, K. Oegema, F. Barron, B. R. Goldsmith, Sensors and Actuators B: Chemical, 2016.

19. N. J. Kybert, G. H. Han, M. B. Lerner, E. N. Dattoli, A. Estandiar, A. T. Charlie Johnson, Nano Res, 2014, 7, 95-103.

20. L. Gao, W. Ren, H. Xu, L. Jin, Z. Wang, T. Ma, L.-P. Ma, Z. Zhang, Q. Fu, L.-M. Peng, X. Bao, H.-M. Cheng, Nature Communications, 2012, 3, 699.

21. J. W. Smith, D. A. Cheresh, The Journal of Biological Chemistry, 1988, 263, 18726-18731.

22. J. W. Smith, D. A. Cheresh, The Journal of Biological Chemistry, 1990, 265, 2168-2172.

23. L. Zhang, H. Jin, X. Guo, Z, Yang, L, Zhao, S. Tang, P. Mo, K. Wu, Y. Nie, Y. Pan, D. Fan, Clinical Biochemistry, 2012, 45, 1064-1069.

CHAPTER 7. SUMMARY AND CONCLUSION

Controlling and studying nanoscale bioparticles is an essential part of many biological fields including drug design (1,2), disease biomarker detection (3), and bioparticle separation (4-8). There are many available methods for this including Förster resonance energy transfer (FRET) (9) and x-ray crystallography (10).

However, these existing methods have some deficiencies. Specifically, population averaging and fluorophore bleaching effects that make distinguishing individual biomaterial kinetics impossible using optical and fluorescence methods (11,12). At the same time, dynamic measurements are extremely difficult via crystallography methods.

Nano-electronics, on the other hand, offer improvements to these techniques (3,13). Interlocking electrodes can be used to apply an AC field throughout a buffer solution and quickly sort and manipulate the positions of bioparticles. At the same time, nano-circuits have been designed to take advantage of the surface sensitivity of carbon nanotubes and graphene to detect and monitor individual proteins and exosomes at a much higher rate of data collection and for much longer durations of time.

This thesis focused on novel developments in these areas of nano-electronics. Firstly, it presented a cutting edge form of atomic force microscopy created to directly measure dielectrophoresis forces applied by interlocked electrodes. This had never been accomplished before on the nanoscale, but the method presented here was successfully used to map these forces by simulating a nanoparticle being acted on by these forces.

Additionally, this thesis focused on several nano-transistor technologies used to directly probe single protein dynamics and detect pancreatic cancer biomarkers at levels present in human patients. Two different proteins (MMP1 and HDAC8) were analyzed using carbon

nanotube field effect transistors. Due to the CNT-transistor ability to take kinetic data from individual proteins at hundreds of thousands of points per second, novel insights on both of these proteins were obtained. In the case of MMP1, it was observed that the kinetic rates are highly dependent on the substrate's structure, leading to new information for the improved design of lipopeptides for MMP-targeting drug delivery.

The HDAC8 observations also lead to important insights on the enzyme's motions, namely: [1] large conformational dynamics occurs between two states that exist in the complex; [2] the binding affinity of the weak inhibitor/ligand to the site pocket is greatly improved by the small molecule activator; [3] only one step rate-limits the closed loop conformation; and [4] after open loop conformation, at least two rate-limiting steps occur that either release the aftermath of the cleavage, or reposition the ligand.

Lastly, a graphene field-effect transistor nano-circuit was used to detect exosomes released from pancreatic cancer tumors. This method was proven effective at sensitively and selectively detecting pancreatic cancer exosomes, and was effective at distinguishing a blood sample from a patient with pancreatic cancer from a blood sample from a healthy patient. These results are promising, but there are still some improvements that can be made in this area. One such improvement would be to perform tests on many more patient samples to get better statistics on our methods ability to diagnose people with pancreatic cancer. Additionally, more tests must be done on samples from patients with early stages of pancreatic cancer to confirm that our method could be used for the early detection that could save a large number of lives.

7.1. References

1. J. Banerjee, A. J. Hanson, B. Gadam, A. I. Elegbede, S. Tobwala, B. Ganguly, A. V. Wagh, W. W. Muhonen, B. Law, J. B. Shabb, D. K. Srivastava and S. Mallik, Bioconjugate Chemistry, 2009, 20, 1332-1339.
2. J. Banerjee, A. J. Hanson, E. K. Nyren-Erickson, B. Ganguli, A. Wagh, W. W. Muhonen, B. Law, J. B. Shabb, D. K. Srivastava and S. Mallik, Chemical Communications, 2010, 46, 3209-3211.
3. A. K. Manoharan, S. Chinnathambi, R. Jayavel, N. Hanagata, Science and Technology of Advanced Materials, 2016, 18, 43-50.
4. R. Pethig, Crit. Rev. Biotechnol, 1996, 16, 331–348.
5. H. Morgan, M. P. Hughes, and N. G. Green, Biophys. J, 1999, 77, 516–525.
6. H. Li and R. Bashir, Sens. Actuators B, 2002, 86, 215–221.
7. C.-F. Chou, J. O. Tegenfeldt, O. Bakajin, S. S. Chan, E. C. Cox, N. Darnton, T. Duke, and R. H. Austin, Biophys. J, 2002, 83, 2170–2179 (2002).
8. M. Washizu and O. Kurosawa, IEEE Trans. Ind. Appl, 1990, 26, 1165–1172.
9. S. Matsumoto, G. G, Hammes, Biochemistry, 1975, 14, 2, 214-224.
10. J.-P. Xiong, T. Stehle, R. Zhang, A. Joachimiak, M. Frech, S. L. Goodman, M. A. Arnaout, Science, 2002, 296, 5565, 151-155.
11. Y. Choi, I. S. Moody, P. C. Sims, S. R. Hunt, B. L. Corso, D. E. Seitz, L. C. Blaszcazk, P. G. Collins and G. A. Weiss, J. Am. Chem. Soc., 2012, 134, 2032.
12. M. V. Akherov, Y. Choi, T. J. Olsen, P. C. Sims, M. Iftikhar, O. T. Gul, B. L. Corso, G. A. Weiss, P. G. Collins, ACS Chem. Biol., 2015, 10, 1495-1501.

13. A. V. Vlassoz, S. Magdaleno, R. Setterquist, R. Conrad, Biochimica et Biophysica Acta (BBA)-General Subjects, 2012, 1820, 940-948.